POLITECNICO DI TORINO

Master's Degree in Aerospace Engineering

Optimal Ascent Trajectories to Sun-Synchronous Orbits via Indirect Methods

Supervisor:
Prof. Manuela Battipede

Co-Supervisor:
Dr. Luigi Mascolo

Author:
Giuseppe De Bari

Academic Year 2024

If you ever feel like you don't fit in, just remember that you're not alone.
We're all in this together, under the same sky.

Abstract

This research aims to optimize ascent trajectories for satellite launches into Sun-Synchronous Orbits (SSO) while minimizing propellant usage during launch to maximize payload capacity. The study evaluates various launch sites and directions, incorporating the multi-stage dynamics of the launch vehicle to accurately model the ascent trajectories and different mission launch times to evaluate performance in regard to the final Local Time of Ascending Node (LTAN) that the insertion orbit should have.

The optimization technique employs an indirect method rooted in optimal control principles and Pontryagin's Maximum Principle, aiming to identify a trajectory that maximizes the Hamiltonian, thereby minimizing propellant use. Considering the vehicle's proximity to Earth during launch and orbital insertion, the dynamical model incorporates Earth's gravitational effects and uses the Harris-Priester Atmospheric Density Model to accurately account for atmospheric drag under aerothermodynamic constraints.

A tailored scenario was created to simulate the ascent of a launch vehicle aimed for insertion into a Low Earth SSO. This simulation was structured to determine the necessary co-states for deriving optimal control solutions. Results indicate that variations in launch site significantly influence propellant use, thereby impacting the payload capacity deliverable to orbit. Furthermore, although the optimal ascent trajectory exhibits consistent characteristics, it is significantly affected by the chosen atmospheric drag model and the specific local time of ascending node (LTAN) settings.

Contents

List of Figures

List of Tables

Acronyms

BC   Boundary Condition

BVP   Boundary Value Problem

DC   Differential Corrector

DM   Direct Method

CoV   Calculus of Variations]

2BM   2-Body Model

2BP   2-Body Problem

4BP   Four-Body Problem

AN   ascending node

DCM   Direction Cosine Matrix

DN   descending node

ECEF   Earth-Centred Earth-Fixed

ECI   Earth-Centred Inertial

EME2000   Earth Mean Equator and Equinox of Epoch J2000

EoM   Equations of Motion

GEO   Geostationary Orbit

HBVP   Hamiltonian Boundary Value Problem

HMPBVP	Hybrid Multi-Point Boundary Value Problem
ICRF	International Celestial Reference Frame
IM	Indirect Method
LAT	Latitude
LEO	Low Earth Orbit
LONG	Longitude
LTAN	Local Time of Ascending Node
MEO	Medium Earth Orbit
MLTAN	Mean Local Time of Ascending Node
MPBVP	Multi-Point Boundary Value Problem
nBP	n-Body Problem
NL	Non Linear
OC	Optimal Control
OCP	Optimal Control Problem
OCT	Optimal Control Theory
ODE	Ordinary Differential Equation
PMP	Pontryagin's Minimum Principle
PmP	Pontryagin's Maximum Principle
RAAN	right ascension of the ascending node
RF	Reference Frame
RS	Reference System
SC	Spacecraft
SSO	Sun Synchronous Orbit

Acronyms

STM	State Transition Matrix
TPBVP	Two-Point Boundary Value Problem
ZEN	Zenith-East-North

Chapter 1

Introduction

The observation of the heavens has evoked in humans a profound sense of wonder, which has manifested itself as an undying curiosity throughout the ages, driving them toward the pursuit of knowledge and the exploration of the mysteries hidden within the universe. This impulse was particularly felt by Galileo Galilei, who, in the 17th century, gave way to some of the most revolutionary discoveries in the field. He was the first to observe the moons of Jupiter and one of the first to take a detailed look at the surface of the moon, anticipating and expanding on the fascination felt by us all for our dreary satellite. Later, Johannes Kepler laid the foundations for future space exploration with his laws of planetary motion, which were essential for understanding the orbits of the planets. In the early 20th century, Konstantin Tsiolkovsky revolutionized astronautics with his theory of liquid-fuelled rockets [1]. He anticipated key concepts essential for space access and developed fundamental relationships which are still used today.

These incredible breakthroughs, which can be said to constitute the pillars of the field, paved the way for rocket propulsion and for future advances in exploration beyond the Earth's atmosphere. Tsiolkovsky's innovative work inspired Robert H. Goddard, who built and successfully launched the first liquid propellant rocket in 1926. This marked the beginning of the modern era of space exploration. These developments charted a course from astronomical observation to humanity's conquest of space exploration.

Access to space marked a revolutionary chapter in the history of mankind. It encouraged ambitious initiatives to explore beyond frontiers that had previously

only been imagined. In addition to the ideological and military struggle between the United States and the Soviet Union during the cold war, a deep interest in science and technology also fuelled these ambitions. Once tensions had died down after the election of president Gorbačëv the once opposing nations used advanced missile technologies that had been extensively probed during the war to develop vehicles capable of carrying payloads into space. This geopolitical rivalry acted as a catalyst for the development of space exploration, which accelerated technological progress and pushed human ambitions beyond the simple placement of satellites in orbit to missions involving the launch of living beings into space.

This period witnessed significant historical events, starting with the launch of Sputnik 1 by the USSR in 1957, which marked the beginning of the artificial satellite era. This was followed by a historic milestone in 1961 with Yuri Gagarin aboard Vostok 1, becoming the first human in orbit. Another defining moment was NASA's Apollo 11 mission in 1969 [2], which fulfilled humanity's age-old dream of landing the first men on the Moon. Other relevant achievements include the launch of Skylab in 1973, the first American space station, and the Voyager 1 and Voyager 2 probes in 1977, sent to explore the planets at the edge of the solar system. Lastly, the deployment of the Hubble Space Telescope in 1990 opened new horizons in astronomical observation, providing unprecedented high-quality images of the universe [3]. Since then, these missions have been the subject of considerable media interest and the catalyst for unprecedented advances in scientific knowledge.

The exploration of space in the 20th century was made possible by the significant contributions of eminent engineers who were involved in the development of the first ballistic missiles. During this period, only the United States and the Soviet Union had the technological capabilities for undertaking space launches. Werner von Braun's 1944 V-2 rocket made history being the first rocket to achieve suborbital flight. In 1957, in the Soviet Union, Sergei Korolev developed the R-7 Semyorka, used to put Sputnik into orbit. In the United States, von Braun led the development of the Saturn V in 1967, crucial for the Apollo missions. In 1981, the Space Shuttle programme was launched and marked a further step forward with the introduction of reusable space vehicles [4]. Over time, several other countries, such as Europe, China, India, Israel, Japan, and Korea, have expanded their capabilities by developing autonomous launchers. The space exploration landscape has been enriched by private companies such as SpaceX with its Falcon 9 [5] and Blue Origin with its New Glenn [6]. Their

significant innovations, including reusable rockets, have transformed space access into a more affordable and sustainable endeavour.

Aerospace research and development has resulted in the creation of advanced launch vehicles capable of carrying large and heavy payloads. The designs of these launchers have evolved over time, adopting new shapes, sizes, and particularly a multi-stage structure. This approach, featuring multiple stages with independent engines, activated at different stages of flight, has been able to optimise fuel consumption and increase overall launch efficiency to previously unattained levels.

(Years in Service) Rocket Name	(1960-1991) VOSTOK-K	(1960-1961) REDSTONE MRLV	(1963-1976) VOSKHOD	(1964-1966) TITAN II GLV	(1966-present) SOYUZ	(1966-1975) SATURN 1B	(1967-1973) SATURN V	(1981-2011) STS	(2002-present) LONG MARCH 2F	(2013-present) FALCON 9	SLS	ANGARA 5P
Number of Manned Missions	6	2	2	10	124	4	10	135	5	–	–	–
Number of Humans Launched	6	2	5	20	218	15	26	355	12	–	–	–
Payload to Low Earth Orbit	4752kg	Suborbital	5900kg	3100kg	7100kg	21000kg	127000kg	24400kg	8400kg	13150kg	70000kg / 130000kg	28500kg

Fig. 1.1 Sketch of some launch vehicles

These changes, characterised by a wider and more diverse approach to space exploration, have ushered in a new era of commercial and private research endeavours. The ongoing technological advances in the space sector have made it possible to develop bold projects, ranging from space tourism to the prospect of colonising Mars. These initiatives have managed to capture the interest of the public and motivate numerous generations to explore the limitless possibilities of space exploration.

Nevertheless, despite the existence of many innovative projects, challenges and constraints must be addressed. A critical issue is the relationship between the capacity of the payload and the amount of propellant needed to reach orbit, which are interdependent factors having a direct impact on the scope of the missions.

These dynamics prompt the question of the feasibility of space exploration and highlight the need for targeted research to investigate all aspects of missions, with a particular focus on the launch phases, which are critical for the mission success.

1.1 Motivations and Objectives

This thesis explores the design and optimization of ascent trajectories with the aim of maximizing the payload that can be transported into orbit through the integration of optimization techniques.

The objective of the current study is to analyse the ascent trajectory of a launcher from defined geographic coordinates - latitude (LAT) and longitude (LONG) - in relation to its launch base. This analysis then proceeds to the positioning of the spacecraft (SC) in a predefined orbit, specifically, Sun-Synchronous Orbits (SSOs), which were chosen from various Low Earth Orbits (LEOs) due to their distinctive characteristics. The advantageous possibility offered by SSOs is that they permit the SC to fly over specific areas of the planet at the same local time with each pass. The international scientific community has evaluated this capability with particular reference to its potential applications in Earth observation missions. The stability of lighting conditions in the observed areas allows SSOs to be employed efficiently for global coverage, enabling extensive mapping of the Earth's surface. Furthermore, their nature allows repeated observation of specific regions, making them invaluable tools for monitoring environmental changes over time.

The undeniable advantages offered by SSOs have permitted the launch of a wide variety of space missions with diverse objectives. These include the monitoring of ocean dynamics, climate variables, terrestrial ecosystems, and global security. The deployment of numerous satellites with the capacity to maintain constant vigilance over the planet has been prompted by the desire of prominent space agencies such as ESA, NASA, JAXA, CSA and CNES to meticulously record every change on the earth's surface. In this context, these agencies, in addition to undertaking

extensive collaborative initiatives with various private entities, including SpaceX, have successfully executed numerous missions that have made space more accessible. The growing interest in SSOs can be evidenced by a number of emblematic examples of mission programs, including the Copernicus Sentinel Program, the EOS AM & PM missions, JPSS, Calypso, Sentinel-6, SAOCOM, RADARSAT, ICEYE, and many others.

The principal challenge of this study is the modelling of an ascent trajectory. The dynamic model employed analyses the gravitational effect of the Earth on the launcher, narrowing down on a simplified version of the problem regarding the interaction of many celestial bodies. Furthermore, the model incorporates the most influential effect, namely drag perturbation due to Earth's atmosphere. By adopting the Harris-Priester atmospheric model, density can be more effectively taken into account for the drag computation. This in turn permits a better description of the launcher performance and allows the study to reflect the reality of the case more faithfully. Launch vehicle utilizes chemical propulsion, in light of that all the manoeuvres will be treated as impulsive. This approach facilitates the simulation of the launcher's stage , a crucial aspect for ensuring efficient access to space. Efficiency gains are achieved through the progressive reduction of the launcher's total mass, which optimizes the use of propellant. Furthermore, the modularity of each of the stages allows for greater flexibility in the configuration of the engines, thus enabling them to be adapted to the mission-specific requirements. In addition, the stage separation enhances safety and reliability, as it reduces the associated risks with the residual propellant.

In this complex context, the primary objective is to identify the optimal trajectory among the various possible options, distinguishing the best solution from suboptimal ones. To this end, it is crucial to employ advanced numerical methods for the analysis of continuous-time optimization problems, which provide guidance on how to enhance suboptimal solutions. In this thesis, the optimization of a trajectory is performed with indirect methods (IM) based on Optimal Control Theory (OCT). These methods, which will be explored in greater detail in subsequent chapters, aim to efficiently identify local optima with robust convergence properties. This approach allows for the identification of the most relevant local optima, enabling the selection of the global optimum among them. The problem is treated as a Boundary Value Problem (BVP) and is resolved through iterative approaches based on Newton's method [7].

The secondary objective of this study is to compare the outcomes produced by a theoretical model created with actual data obtained from a SpaceX launch, which took place for the ICEYE mission [8]. This analysis is crucial for evaluating the precision of the proposed model by comparing aspects such as propulsive expenditure and timing with those observed during the real mission. The comparison aims to identify discrepancies between the theoretical model and its practical application, by analysing the causes of these discrepancies and quantifying the margin of error. This approach not only validates the model's reliability but also provides critical insights for future enhancements and refinements.

1.2   Thesis Overview

A concise overview of the contents of the thesis is provided herein.

- Chapter 2 explores the dynamic model that governs the evolution of the launch vehicle over time. The chapter opens with a comprehensive examination of the reference systems utilized, subsequently followed by an exposition on fundamental astrodynamic concepts. Subsequently, theoretical concepts that are essential for comprehending the model are addressed, including the n-body problem and its simplified case, ascent models and sun-synchronous orbits. Moreover, the chapter introduces the primary perturbative effect considered in the context of a medium-fidelity model.

- Chapter 3 provides an overview of optimal control theory, including both direct and indirect methods. It demonstrates the numerical instruments utilised for solving optimisation problems and examines the theoretical insights offered by indirect methods, along with specific algorithms and operations designed to enhance method convergence. Finally, it explores the practical application of the theory in the case study, focusing on the optimisation domain of a launcher's ascent trajectory.

- Chapter 4 provides the essential details on the prescribed initial and final boundary conditions. Furthermore, it analyses the optimum solutions of assorted ascent trajectories obtained by varying the launch point in a Two-Body Problem. The distinct scenarios are presented and discussed with the objective of identifying the optimal launch strategy.

- Chapter 5, in conclusion, presents a comprehensive summary of the work undertaken, highlighting the principal results obtained. In addition, it suggests avenues for future research with the aim of further enhancing the realism and accuracy of the model.

Chapter 2

Dynamic model

Chapter two presents the dynamic model implemented for the analysis of a launch vehicle's ascent to a Sun-Synchronous Orbit (SSO). This study is based on a medium-fidelity model that utilises the two-body motion equations and incorporates one of the most significant perturbative accelerations in the initial phases of flight, namely aerodynamic drag. Furthermore, supplementary considerations were made to implement the staging phase by defining successive thrust arcs and introducing additional details for a more thorough analysis.

The initial section of the Chapter introduces the reference systems that are necessary for accurately describing the motion of the launch vehicle. Subsequently, the following section addresses astrodynamics concepts. It begins with Kepler's laws and proceeds to discuss the n-body problem and its simplification into the two-Body Problem (2BP), along with the resulting closed-form solutions. The third section introduces the equations of motion that describe the evolution of the launch vehicle during ascent. It places particular emphasis on propulsive expenditures and the adopted ascent model, including details related to staging. The fourth section offers insights on SSO, including an analysis of their advantages and the methods for defining and modelling such orbits. Finally, the last section presents information on drag and its incorporation into the dynamic model.

For the sake of clarity, the notation employed throughout this thesis for the clear and concise expression of formulas and equations is explained in detail, unless otherwise specified. The vectors will be presented in lowercase bold font ($\boldsymbol{x}$), with the sole exception of known quantities (e.g., velocity $\boldsymbol{V}$), which will be presented as

column vectors. Instead, unit vectors will be identified through the use of bold letters and a hat ($\hat{\boldsymbol{x}}$). The matrices will be represented using the uppercase bold font ($\boldsymbol{A}$). Time derivatives, for both scalars and vectors, will be marked with one or multiple dots depending on the order of derivation ($\dot{x}$, $\ddot{x}$, $\dot{\boldsymbol{x}}$, $\ddot{\boldsymbol{x}}$). Moreover, Greek letters are used to express angles and other quantities. Lastly, to indicate those quantities that have undergone mathematical manipulation, such as non-dimensionalisation, a tilde will be used ($\tilde{x}$, $\dot{\tilde{x}}$, $\ddot{\tilde{x}}$, ...).

2.1 Reference Frames and Systems

A Reference System (RS) is a theoretical concept that establishes the necessary principles for measuring a physical quantity. A generic RS is uniquely defined by three elements: the origin, the fundamental plane, and a set of three orthonormal unit vectors, which form a right-handed positive direction triad, also referred to as the Reference Frame (RF).

Two further concepts are necessary to introduce with regard to inertial and non-inertial RF. The principal distinction between these frames is the presence or absence of additional pseudo-accelerations due to relative observations, such as the Coriolis or centrifugal effects. In an inertial RF, the motion of a body not subjected to external forces is either uniform rectilinear or stationary, maintaining its stability over time. In contrast, within a non-inertial RF, a body experiences accelerations relative to an inertial frame. This necessitates the introduction of apparent forces to accurately describe the motion of bodies, whereby the system results susceptible to dynamic effects. The selection of the most suitable reference frame depends on the nature of the analysis and can potentially facilitate the resolution of problems.

As an illustration, the motion of a body in space relative to the Earth can be described using various RF, employing different sets of coordinates. These include the characteristic quantities of the perifocal RF $\{a, e, i, \Omega, \omega, \nu\}$, or in the EME2000 RF using Cartesian coordinates $\{x, y, z\}$ or polar coordinates $\{r, \vartheta, \varphi\}$.

Three reference systems will be used, as shown in the following image
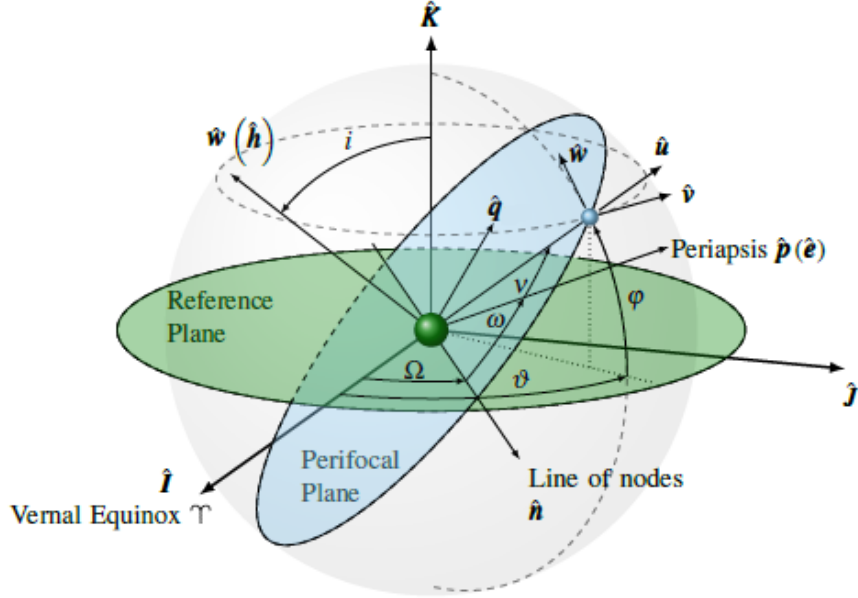
Fig. 2.1 A schematic illustration of the principal Reference Systems: EME2000 $\{\hat{\boldsymbol{I}}, \hat{\boldsymbol{J}}, \hat{\boldsymbol{K}}\}$, perifocal $\{\hat{\boldsymbol{p}}, \hat{\boldsymbol{q}}, \hat{\boldsymbol{w}}\}$, and ZEN $\{\hat{\boldsymbol{u}}, \hat{\boldsymbol{v}}, \hat{\boldsymbol{w}}\}$ RSs [9]

2.1.1   Geocentric-Equatorial RF

This thesis considers the use of a geocentric-equatorial reference system to accurately describe the motion of bodies relative to the Earth. The Earth Mean Equator and Equinox of Epoch J2000 (EME2000) represents a specific type of Earth-Centred Inertial (ECI) frame. It can be considered inertial because it is in close alignment with the International Celestial Reference Frame (ICRF) [10], with any rotational offset between these frames being on the order of hundredths of an arcsecond, which is negligible. The ICRF is an inertial system based on radio astronomical observations, which is used to define the position of celestial bodies on a global scale, including librations and nutations [11].

This RF is centred on the Earth, with the reference plane coinciding with the equatorial plane. The unit vectors $\{\hat{\boldsymbol{I}}, \hat{\boldsymbol{J}}, \hat{\boldsymbol{K}}\}$ are defined as follows: $\hat{\boldsymbol{I}}$ is aligned with the direction of the Vernal Equinox, $\hat{\boldsymbol{K}}$ is perpendicular to the reference plane, and $\hat{\boldsymbol{J}}$ completes the right-handed triad.

10

In contrast, the Earth-Centred Earth-Fixed (ECEF) frame is a non-inertial frame, but the origin remains fixed at the centre of the Earth and the reference plane coinciding with the equatorial plane. The principal distinction between the EME2000 and the ECEF is that the axes in the latter rotate at the same velocity as the surface of the Earth. The right-handed triad in ECEF RF consists of $\hat{\boldsymbol{I}}'$, which points towards the intersection of the equator and the Greenwich meridian, $\hat{\boldsymbol{K}}'$, which is perpendicular to the reference plane, and $\hat{\boldsymbol{J}}'$, which completes the triad.

2.1.2 Perifocal RF

A satellite's motion is described within the perifocal RF, which means that the trajectory of the examined body is located within the perifocal plane relative to the reference body. This RF is centred on the primary gravitational body, namely the Earth, and uses a triad of unit vectors $\left\{ \hat{\boldsymbol{p}}_{body}, \hat{\boldsymbol{q}}_{body}, \hat{\boldsymbol{w}}_{body} \right\}$, as shown in Figure 2.2:
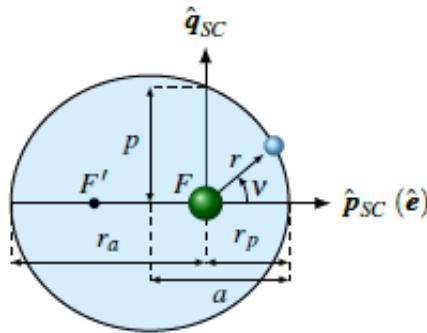
Fig. 2.2 Perifocal RF, with $e = 0.4$, [9]

It is important to specify the direction of these vectors using the Keplerian parameters mentioned in Section 2.2.2. The unit vector $\hat{\boldsymbol{p}}_{body}$ is parallel to the eccentricity vector, $\hat{\boldsymbol{q}}_{body}$ is normal to the orbital plane and aligned with the angular momentum vector $\hat{\boldsymbol{h}}$, while $\hat{\boldsymbol{q}}_{body}$ completes the right-handed triad. As postulated by Kepler's first law, an unperturbed body in this RF will indefinitely follow a trajectory described by a conic section. The geometry and orientation of the orbit are described through a set of parameters, known as classical Keplerian elements $\{a, e, i, \Omega, \omega, \nu\}$, which allow for the identification of the body's position. However, only a restricted number of parameters are necessary to define the perifocal RF.

2.1.3 ZEN RF

The Zenith-East-North (ZEN) RF is a topocentric system associated with the centre of mass of the body under analysis. This rotating, non-inertial RF is defined by the unit vectors $\{\hat{\boldsymbol{u}}, \hat{\boldsymbol{v}}, \hat{\boldsymbol{w}}\}$, representing the body's velocity components in the radial, tangential, and normal directions, respectively. Specifically, the radial direction is defined by extending the body's position vector from the Earth's centre, while the tangential and normal directions align with the directions of the celestial sphere's parallel and meridian. It is notable that the velocity components are neither parallel nor coincident with the orbital velocity vector, which is tangent to the orbital plane.

2.1.4 Coordinate Transformation and Rotation Matrices

A fundamental aspect of coordinate transformation is the projection of the components of a generic vector from the initial RS to the target system, such as

$$\begin{Bmatrix} r_I \\ r_J \\ r_K \end{Bmatrix} = \begin{bmatrix} \hat{\boldsymbol{I}} \cdot \hat{\boldsymbol{p}} & \hat{\boldsymbol{I}} \cdot \hat{\boldsymbol{q}} & \hat{\boldsymbol{I}} \cdot \hat{\boldsymbol{w}} \\ \hat{\boldsymbol{J}} \cdot \hat{\boldsymbol{p}} & \hat{\boldsymbol{J}} \cdot \hat{\boldsymbol{q}} & \hat{\boldsymbol{J}} \cdot \hat{\boldsymbol{w}} \\ \hat{\boldsymbol{K}} \cdot \hat{\boldsymbol{p}} & \hat{\boldsymbol{K}} \cdot \hat{\boldsymbol{q}} & \hat{\boldsymbol{K}} \cdot \hat{\boldsymbol{w}} \end{bmatrix} \begin{Bmatrix} r_p \\ r_q \\ r_w \end{Bmatrix}. \tag{2.1}$$

As illustrated in Equation (2.1), this coordinate transformation is implemented through the use of a simple rotation matrix, which is composed of a series of elementary Direction Cosine Matrix (DCM) represented as follows:

$$\boldsymbol{R}_1(\cdot) = \begin{bmatrix} 1 & 0 & 0 \\ 0 & c\cdot & s\cdot \\ 0 & -s\cdot & c\cdot \end{bmatrix}, \quad \boldsymbol{R}_2(\cdot) = \begin{bmatrix} c\cdot & 0 & s\cdot \\ 0 & 1 & 0 \\ -s\cdot & 0 & c\cdot \end{bmatrix}, \quad \boldsymbol{R}_3(\cdot) = \begin{bmatrix} c\cdot & s\cdot & 0 \\ -s\cdot & c\cdot & 0 \\ 0 & 0 & 1 \end{bmatrix}. \tag{2.2}$$

For instance, to perform a coordinate transformation from the EME2000 RF to the perifocal RF, elementary rotations around each axis are required, as highlighted in Figure 2.3. Therefore, the first rotation must be executed around the $\hat{\boldsymbol{K}}$ axis by an angle Ω,

$$\boldsymbol{r}_{I'J'K} = \boldsymbol{R}(\Omega)\boldsymbol{r}_{IJK}, \tag{2.3}$$

which results in a rotation of the $\hat{\boldsymbol{I}}'$ axis, aligning it with the line of nodes $\hat{\boldsymbol{n}}$. Subsequently, a second elementary rotation around the newly formed $\hat{\boldsymbol{I}}'$ axis will be

performed by an angle i,

$$\boldsymbol{r}_{I''J''K'} = \boldsymbol{R}(i)\boldsymbol{r}_{I'J'K}, \tag{2.4}$$

which aligns the $\hat{\boldsymbol{K}}$ axis with the $\hat{\boldsymbol{w}}$ unit vector. The final rotation, by an angle ω around the new $\hat{\boldsymbol{K}}'$ axis,

$$\boldsymbol{r}_{pqw} = \boldsymbol{R}(\omega)\boldsymbol{r}_{I''J''K'}, \tag{2.5}$$

will complete the right-handed triad, aligning $\hat{\boldsymbol{I}}''$ with $\hat{\boldsymbol{p}}$ and $\hat{\boldsymbol{J}}'''$ with $\hat{\boldsymbol{q}}$. In practice, the 3-1-3 elementary rotation sequences are not applied individually, but rather the complete rotation matrix following the Euler sequence is utilised. This results in

$$\boldsymbol{r}_{pqw} = \boldsymbol{R}_{313}(\Omega, i, \omega)\boldsymbol{r}_{IJK}. \tag{2.6}$$

As previously described, it is possible to transpose from the EME2000 RF to the ZEN RF. The difference lies in the sequence of elementary rotations, which are 2-3, resulting in

$$\boldsymbol{r}_{ZEN} = \boldsymbol{R}_{23}(\varphi, \vartheta)\boldsymbol{r}_{IJK}. \tag{2.7}$$
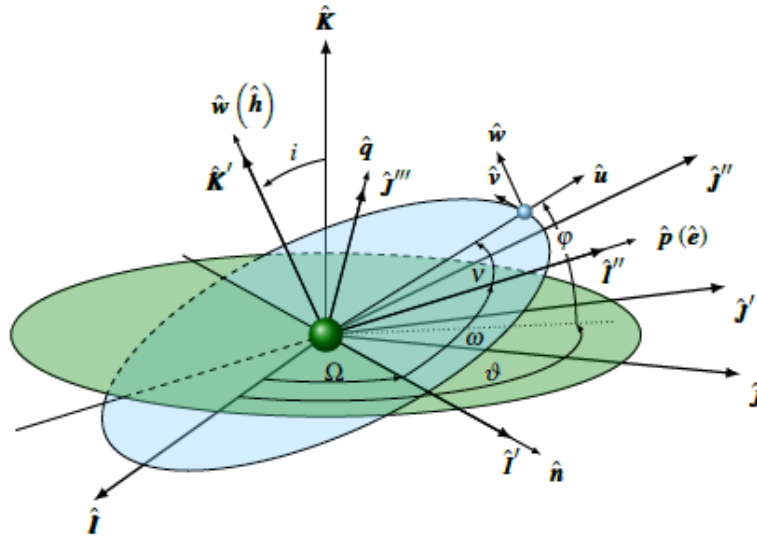
Fig. 2.3 Elementary Rotations around the axes of the EME2000 RF $\{\hat{\boldsymbol{I}}, \hat{\boldsymbol{J}}, \hat{\boldsymbol{K}}\}$ to transform to the perifocal RF $\{\hat{\boldsymbol{p}}_{body}, \hat{\boldsymbol{q}}_{body}, \hat{\boldsymbol{w}}_{body}\}$, [9]

Inverse rotations can be easily computed using the transposed DCMs, due to their orthonormality.

2.2   General Principles of Orbital Mechanics

Space mechanics is an area within the broader field of science concerned with the movement of objects in space under the influence of gravity. This field may be divided into two categories: astrodynamics, which concerns the study of SC motion, and celestial mechanics, which deals with the motion of celestial bodies such as planets and asteroids.

The theoretical foundations of orbital mechanics are primarily based on Kepler's laws, which are briefly stated below.

- The *first law* defines the geometric shape of an orbit as an ellipse. Consequently, planets move in elliptical orbits with the Sun located at one of the two focal points, as illustrated in Figure 2.4. This observation is derived from the fact that the distance between the Sun and the planet is not constant throughout their orbit. Specifically, there is a point in the orbit where the Sun and the planet are closest together, called the *perihelion*, and another point where they are furthest apart, called the *aphelion*.
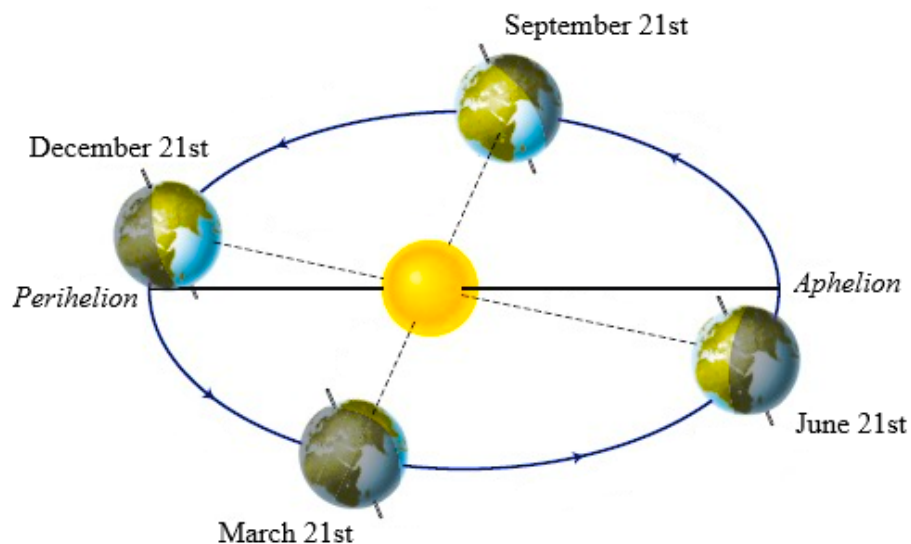
Fig. 2.4 Earth's motion in an elliptical orbit with the Sun at one focus

- The *second law* states that the same areas within an ellipse are swept by the line connecting the Sun and the planet in equal times. This observation is predicated on a mathematical conjecture stipulating that angular velocity of

14

the planet is greater when it is at perihelion and lesser when it is at aphelion. The orbital period is defined as the requisite time required to sweep out the total surface area of the ellipse.

- The *third law* defines the relationship between the motions of different planets in the solar system. It states that there is no variation in the ratio between the squares of planetary orbital periods and the cubes of planetary mean distances from the sun, which is constant for all planets in our solar system.

Although Kepler's laws provide insight into the behaviour of planetary orbits, they do not explain why planets move as they do. This is because the concept of the gravitational force, introduced by Newton in the XVII century, was absent from Kepler's work. Newton's laws not only explain Kepler's observations but also provide a unified theoretical basis for understanding all gravitational interactions. Consequently, the dynamic model of the motion of bodies in space is described using a combination of Newton's laws, which form the basis of modern physics. In particular, the second law of motion,

$$\boldsymbol{F} = \frac{d}{dt}(m\boldsymbol{v}), \tag{2.8}$$

highlights the interrelationship between the external forces acting upon a body and the time variation of its momentum, as observed from an inertial reference frame. Furthermore, Newton's law of universal gravitation,

$$\boldsymbol{F} = -G\,\frac{m_1 m_2}{r^2}\,\frac{\boldsymbol{r}}{r}, \tag{2.9}$$

states that two material points with masses m_1 and m_2 exert an attractive force on each other along the line connecting them. The magnitude of this force is directly proportional to the product of the two masses and inversely proportional to the square of their distance. The parameter G is the universal gravitational constant, which has a value of $6.67259 \cdot 10^{-11} m^3\ kg^{-1}\ s^{-2}$.

The integration of Kepler's laws with Newton's second law of motion and the law of universal gravitation offers a thorough understanding of orbital dynamics. This combination forms the basis of orbital mechanics, providing a robust foundation for space navigation. For a more in-depth explanation, refer to Conway's book [12].

2.2.1 The n-Body Problem

The n-Body Problem (nBP) is one of the most challenging problems in astrodynamics. This problem is of particular interest because, in order to study a dynamical system as close to reality as possible and to obtain accurate results, it is essential to take into account all perturbative effects from other bodies in the solar system that interact with the body under study. Consequently, in order to conduct a comprehensive and precise trajectory analysis, it is essential to integrate these effects into the model utilising the JPL DExxx planetary ephemerides, which are provided by NASA's Navigation and Ancillary Information Facility [11]. These ephemerides enable the prediction of the positions of various celestial bodies over time with high precision.

The problem can thus be stated as follows: given the initial positions and velocities of bodies with known masses, the objective is to determine these quantities at any other point in time. Accurately defining these quantities enables a clearer understanding of celestial dynamics, thereby facilitating the analysis of gravitational effects on satellites during space manoeuvrers.

In the context of an nBP, a non-rotating reference system is employed, allowing for a more straightforward and useful definition of the problem. In this dynamic model, the n bodies evolve into their successive states, mutually influencing each other. Here, the Earth is considered the primary body relative to which the ephemerides are calculated, utilising as a RS the EME2000. Within this framework, the Earth is designated as the k-th body among the j-th bodies, while the body under examination, namely the SC, is denoted by i.
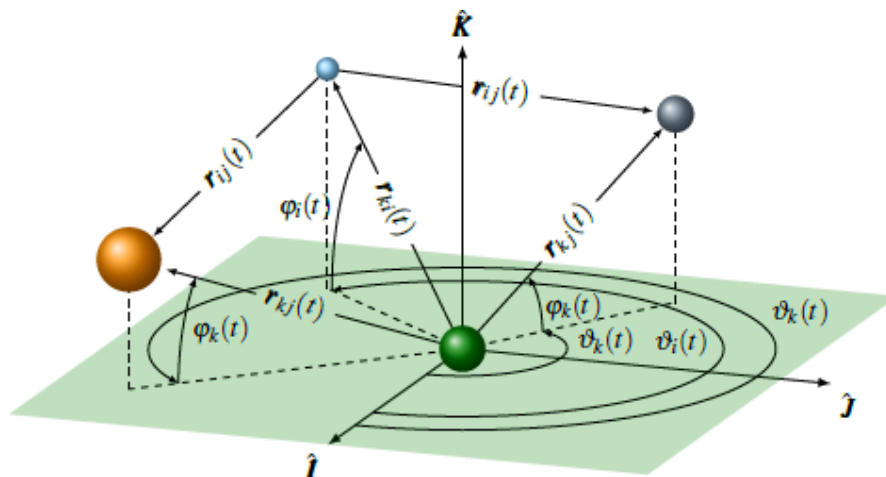
Fig. 2.5 Schematic representation of n-Body Problem in EME2000 RF, [9]

Figure 2.5 provides a schematic representation of the RF in the nBP. The acceleration of the i-th body relative to the k-th central body of the RF can be expressed as a second-order ODE, specifically

$$\ddot{\mathbf{r}}_{ki} = -\frac{(\mu_i + \mu_k)}{r_{ki}^3}\mathbf{r}_{ki} + \sum_{\substack{j=1 \\ j \neq i,k}}^{n} \mu_j \left(\frac{\mathbf{r}_{ij}}{r_{ij}^3} - \frac{\mathbf{r}_{kj}}{r_{kj}^3} \right). \tag{2.10}$$

The position of the body $\boldsymbol{r}_{ki}$ is calculated through integration during the analysis, whereas the positions of the other bodies $\boldsymbol{r}_{kj}$ are known relative to the Earth in the ICRF and are provided by the DExxx JPL ephemerides in Cartesian coordinates (x_{kj}, y_{kj}, z_{kj}). Finally, the relative positions $\boldsymbol{r}_{ij}$ of the vectors used to compute the perturbative effects due to the gravitational influences of other bodies on the SC are obtained through vector subtractions

$$\boldsymbol{r}_{ij}(t) = \boldsymbol{r}_{kj}(t) - \boldsymbol{r}_{ki}(t). \tag{2.11}$$

Although the problem can be formulated, closed-form analytical solutions are not available for $n > 2$. The system is highly non-linear and sensitive to even small variations in initial conditions due to the complex gravitational interactions. This complexity necessitates the use of numerical methods to obtain approximate solutions to the problem. Various numerical methods can be employed, but they require significant computational effort and careful error management, especially for simulations involving a large number of bodies or extended time periods.

2.2.2 2-Body Problem

A specific case of the nBP, obtained by appropriate simplifying assumptions that reduce the model's dimensions, is the two-Body Problem (2BP). In the 2BP, the mutual interaction between the primary body and the target body is considered, while the gravitational effects of other bodies are neglected. As a consequence, the dynamical model no longer exhibits intricate interactions between multiple bodies but instead focuses on two: the primary body M, which is Earth, and the spacecraft m, with the condition of $M \gg m$. Despite the simplicity of the Two-Body Model (2BM), it leads to particularly interesting solutions due to the existence of an analytical closed-form solution, which allows the trajectory of the bodies to be determined.

In order to derive the equation of motion in a 2BP, an inertial RF (X', Y', Z') is considered. Within this RF, the distances between the origin, the Earth $\boldsymbol{r}_M$, and the SC $\boldsymbol{r}_m$ are uniquely measurable. Additionally, a non-rotating system centred on the primary body with axes parallel to (X', Y', Z') is taken into account, namely the EME2000 RF. By applying Newton's second law to both bodies, the resulting equations are obtained

$$m\ddot{\boldsymbol{r}}_m = -G\,\frac{m\,M}{r^2}\frac{\boldsymbol{r}}{r} \tag{2.12a}$$

$$M\ddot{\boldsymbol{r}}_M = +G\,\frac{m\,M}{r^2}\frac{\boldsymbol{r}}{r}, \tag{2.12b}$$

where the relative distance is

$$\ddot{\boldsymbol{r}} = \ddot{\boldsymbol{r}}_m - \ddot{\boldsymbol{r}}_M = -G\,\frac{m+M}{r^2}\frac{\boldsymbol{r}}{r}. \tag{2.13}$$

Equation (2.13) represents the second-order vector ODE that describes the motion of the secondary body relative to the primary body in the 2BP, where the acceleration is exclusively radial. Given that $m \ll M$, m is considered negligible, and $\mu = G\,M$ is the gravitational constant, which for Earth is $3.98633 \cdot 10^5 m^3\ s^{-2}$. Consequently, the previous equation can be reformulated as follows:

$$\ddot{\boldsymbol{r}} = -\frac{\mu}{r^3}\,\boldsymbol{r}. \tag{2.14}$$

Before deriving the analytical expression of the trajectory, it is essential to introduce some constants of motion that are of particular interest. By performing the vector multiplication of Equation (2.14) with the vector $\boldsymbol{r}$, it can be written

$$\boldsymbol{r} \times \ddot{\boldsymbol{r}} + \boldsymbol{r} \times \frac{\mu}{r^3}\,\boldsymbol{r} = 0, \tag{2.15}$$

from which the following is obtained

$$\frac{d}{dt}(\boldsymbol{r} \times \dot{\boldsymbol{r}}) = 0. \tag{2.16}$$

As a consequence of the previous equation, the first important constant of motion can be stated as

$$\boldsymbol{r} \times \boldsymbol{v} = \boldsymbol{h} = cost. \tag{2.17}$$

The quantity just determined is defined as the angular momentum $\boldsymbol{h}$, and it remains constant throughout the entire trajectory. Therefore, the entire motion field is contained within the plane of the orbit, specifically the perifocal plane, rendering the trajectory planar with respect to the primary body.

The second important constant of motion, derived from the 2BP, is the specific mechanical energy $\mathscr{E}$, which remains constant in each orbit. This quantity can be expressed as

$$\mathscr{E} = \frac{v^2}{2} - \frac{\mu}{r} = cost, \qquad (2.18)$$

where the first term represents the specific kinetic energy and the second term represents the specific potential energy. Further considerations led to the formulation of the SC's specific energy in relation to the shape of its orbit:

$$\mathscr{E} = -\frac{\mu}{2a} = cost. \qquad (2.19)$$

The value of $\mathscr{E}$ determines the nature of the orbit. In particular, if $\mathscr{E} < 0$, the orbit is closed, as in the case of an ellipse or a circle. Conversely, if $\mathscr{E} \geq 0$, the orbit is open, resulting in a parabola if $\mathscr{E} = 0$ and a hyperbola if $\mathscr{E} > 0$.

The equation of motion can now be integrated in order to determine the trajectory of the SC. However, this process requires certain mathematical manipulations, and equation 2.15 is therefore first to be vectorially multiplied by $\boldsymbol{h}$ and subsequently integrated over time. This results in

$$\boldsymbol{h} \times \dot{\boldsymbol{r}} = \frac{\mu}{r}\boldsymbol{r} + B, \qquad (2.20)$$

where B is a constant of integration. This procedure transforms a second-order ODE into a first-order ODE. Further manipulations are necessary to derive the analytical relation of the trajectory in the 2BP. In particular, Equation (2.20) is pre-multiplied scalar by $\boldsymbol{r}$, which gives rise to the expression:

$$r = \frac{\dfrac{h^2}{\mu}}{1 + \dfrac{B}{\mu}\cos(v)}. \qquad (2.21)$$

Following the previously established relationships, it is possible to advance several significant considerations. Given an ellipse, the distance of an arbitrary point from one of its focal points can be calculated in the following manner:

$$r = \frac{a(1-e^2)}{1+e\cos(v)}. \tag{2.22}$$

As can be observed, the analogies between Equations (2.21) and (2.22) confirm Kepler's first law, implying that the trajectory equation is accurately described by that of an ellipse. Since the orbits are closed, a series of parameters is required to describe them. The first parameter is the semi-major axis a, which defines the size of the orbit, while the second parameter is the eccentricity e, which describes its shape by measuring the deviation from a circular orbit. These two Keplerian parameters are related through the *semilatus-rectum p*, according to the formula $p = a(1-e^2)$. Another parameter of particular interest is the true anomaly v, which identifies the angular position of a body relative to the periapsis. The combination of these three parameters $\{a, e, v\}$ allows for a complete identification of the SC's position within the orbit of the perifocal RF.

The remaining three Keplerian parameters are now introduced to identify the orbital plane in a three-dimensional space. Specifically, the orbital plane may be inclined with respect to the reference equatorial plane by an angle i, known as inclination. This inclination results in an intersection between the two planes, giving rise to the line of nodes $\hat{\boldsymbol{n}}$, which marks the transition of the SC from one hemisphere to the other through the ascending node (AN) and the descending node (DN). The direction of $\hat{\boldsymbol{n}}$ coincides with that of the AN and is measured from the $\hat{\boldsymbol{I}}$ axis by the Right-Ascension of the ascending-node (RAAN) Ω. Finally, for a non-circular orbit, the position of the periapsis is identified by the argument of periapsis ω measured from the line of nodes, or from the $\hat{\boldsymbol{I}}$ axis when Ω is undefined, as clearly illustrated in Figure 2.1.

In conclusion, the 2BM is adopted to simulate the launcher's ascent due to the various phases occurring near the Earth, where its gravitational effect is predominant compared to other celestial bodies. Although this model presents substantial differences from reality, it is used for its simplicity in modelling.

2.3 Equations of motion

It is now possible to present the equations of motion which describe the evolution in terms of the position and velocity of the launch vehicle during ascent. As previously highlighted, these equations are represented by a set of ODEs, referenced to a RF centred on the primary celestial body.

In the case of interest, the equations are expressed in the ECEF RF and take the following form:

$$\frac{d\boldsymbol{r}}{dt} = \boldsymbol{V} \tag{2.23a}$$

$$\frac{d\boldsymbol{V}}{dt} = \boldsymbol{g} + \frac{\boldsymbol{T}}{m} + \frac{\boldsymbol{D}}{m} + \mathbf{a}_{cor} + \mathbf{a}_{cf} \tag{2.23b}$$

$$\frac{dm}{dt} = -\frac{T}{c} \tag{2.23c}$$

These equations have already been reformulated in order to accommodate the simplifications that have been applied to the model. Given that they are defined with respect to a non-inertial RF, the effects of apparent forces must be incorporated. As illustrated in the acceleration equation (2.23b), both accelerations can be expressed explicitly as follows:

$$\mathbf{a}_{cl} = \frac{\boldsymbol{F}_{cl}}{m} = -2(\boldsymbol{\omega}_{\oplus} \times \boldsymbol{v}) \tag{2.24a}$$

$$\mathbf{a}_{cor} = \frac{\boldsymbol{F}_{cor}}{m} = -\boldsymbol{\omega}_{\oplus} \times (\boldsymbol{\omega}_{\oplus} \times \boldsymbol{r}) \tag{2.24b}$$

In Equation (2.23c), the variation of mass over time is expressed, thereby allowing the propulsive expenditure to be quantified. In this analysis, the thrust T and exhaust velocity c values are assumed to be constant, thus resulting in a linear mass variation. The dynamic model incorporates a staging mechanism for the launch vehicle, with specific values for these parameters being provided for the operational phases of each stage.

2.3.1 ΔV Calculation and Take-Off Model

Subsequent to the definition of the equations of motion, this section provides a comprehensive examination of the ascent model. The analysis includes an investigation of the associated propulsive expenditure and addresses all aspects related to the launcher and the target orbit. It is first necessary to introduce the fundamental relationship developed by Tsiolkovsky for propulsion, which directly correlates the change in velocity (ΔV) required to reach the desired orbit with the necessary propulsive expenditure, represented by the amount of propellant mass consumed. This relationship is commonly known as the Rocket Equation and is expressed as follows:

$$\Delta V_{vehicle} = c \, \ln \left(\frac{m_0}{m_f} \right) \tag{2.25}$$

where ΔV represents the maximum change of speed that can be attained by the vehicle, c is the effective exhaust velocity, m_0 is the initial mass of the rocket (including the propellant mass), and m_f is the final mass.

The equation (2.25) highlights the interdependence of the performance of a launch vehicle and its capacity to reach the desired orbit on the availability of propellant, as well as the efficiency of the engine. These variables can impose limitations on the feasibility of a space mission, thereby rendering some more complex and challenging to undertake than others. Consequently, the effective result, represented by ΔV, is influenced by practical constraints such as the amount of transportable propellant, the reaction capability, and the engine's performance, which engineers must address. Tsiolkovsky's equation can also be rewritten by explicitly expressing the mass ratio:

$$\frac{m_0}{m_f} = e^{\frac{\Delta V_{vehicle}}{c}} \tag{2.26}$$

From (2.26), it is evident that the quantity of propellant required is contingent not only on the performance of the launch vehicle but also on the desired velocity increment.

During the ascent phase, the launch vehicle's velocity values are required to ensure its lift-off from the ground and continued ascent to orbit. The propellant

expenditure must be considered in light of several contributions:

$$\Delta V_{mission} = V_{orbit} + \Delta V_{gravity} + \Delta V_{drag} + \Delta V_{steering} - \Delta V_{gain} \qquad (2.27)$$

In addition to the costs associated with orbit insertion, it is crucial to consider the impact of gravity and drag losses, which are particularly significant during the initial minutes of ascent. These losses are closely related to the thrust-to-weight ratio (T/W), which must be greater than one for a launch vehicle. A higher T/W ratio allows the vehicle to escape the denser layers of the atmosphere more quickly, although this increases drag losses while reducing gravity losses.

$$\Delta V_{\text{gravity}} = \int_0^t g(t)\,dt \qquad (2.28a)$$

$$\Delta V_{\text{drag}} = \int_0^t \frac{D(t)}{m(t)}\,dt \qquad (2.28b)$$

Additionally, launch vehicles experience other losses due to manoeuvrers and pressure variations during ascent. While these losses are less significant than the previous ones, they contribute to a 5-6 % reduction in the required velocity increment, which must be compensated by propulsive action. Furthermore, the effect of Earth's rotation contributes to an initial velocity gain, reducing the required ΔV. However, this gain varies depending on the latitude (δ) of the launch site:

$$\Delta V_{gain} = \omega_\oplus R \cos(\delta) \qquad (2.29)$$

The ascent trajectory is typically divided into several distinct segments, each characterised by a specific duration and function based on the phase considered. The ascent profile adopted, illustrated in Figure 2.6, begins with a purely vertical ascent phase at $t = 0$. Subsequently, at an altitude of approximately 30 km, a thrust steering manoeuvre, assumed to be instantaneous and useful for varying the direction of the launcher's thrust, is executed to enter the Zero Lift Gravity Turn phase. In this phase, the rotation executed by the launcher along the trajectory is generated by the gravitational force. At approximately 90 km, the Main Engine Cut-Off (MECO) occurs, followed by the separation of the first stage and then the fairing. Once separation has been confirmed, the immediate ignition of the second stage takes place. However, in this particular case study, the aforementioned phases are considered to occur simultaneously, and the reentry of the first stage is not within

the scope of this study. The ascent manoeuvre will be considered complete once the target orbit is reached, where the Second Engine Cut-Off (SECO) will occur.
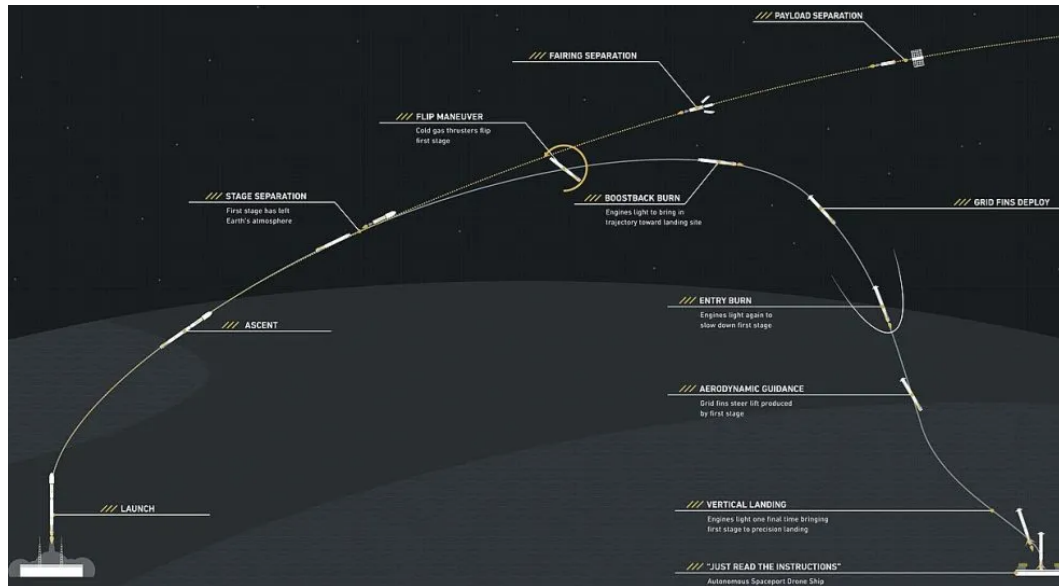
Fig. 2.6 Falcon 9 ascent trajectory and involved phases, [5]

The primary focus of this thesis is to investigate the optimisation of these launch sequences, which define the entire trajectory. The objective is to enhance the overall launch performance, thereby increasing the payload capacity that can be transported into orbit. This improvement in efficiency makes missions more cost-effective and enhances the feasibility of space operations.

2.3.2 Multistage Launcher Design

The staging of a launch vehicle is a crucial aspect to be considered during the design process, as this approach enhances the vehicle's overall efficiency. It involves dividing the vehicle into multiple stages, each equipped with its own engine and propellant. The advantage of this approach lies in the ability to discard parts of the vehicle that are no longer useful for ascent, thereby reducing the mass that needs to be accelerated during subsequent flight phases. Although this results in increased complexity, it allows for the maximum velocity increment to be obtained from the propulsion system and for the maximum payload to be delivered to orbit.

Two fundamental parameters can be introduced

$$\varepsilon_j = \frac{m_{tank,j}}{m_{tank,j} + m_{prop,j}} \tag{2.30a}$$

$$\lambda_j = \frac{m_{pl,j}}{m_{tank,j} + m_{prop,j}} \tag{2.30b}$$

The first of these is the structural ratio, which measures the amount of structure in the stage. This parameter includes the mass of the structures, mechanisms, engines, fuel tanks, control and measurement systems, excluding the propellant and payload. The second parameter is the payload fraction, which represents the ratio of the payload to the total mass of the system.

In the analysis of an N-stage launch vehicle, the payload associated with the j-th stage can be considered as the initial mass of the subsequent stage, namely

$$m_{f,j} = m_{0,j+1}. \tag{2.31}$$

This introduces the concept of a sub-rocket, which has significant implications, demonstrating that each sub-rocket is not only responsible for the weight of its own payload, but also for that of all subsequent stages, as illustrated in Figure 2.7.
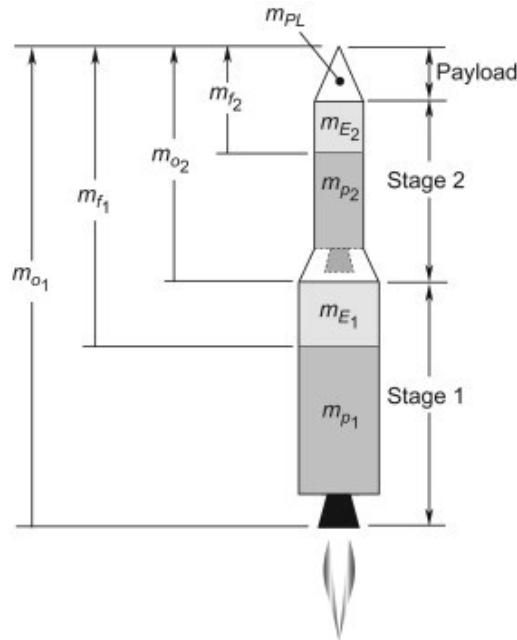
Fig. 2.7 Subdivision in series of a multi-stage launcher

The velocity increment for each stage is calculated according to the rocket equation (2.25). In the case of a multistage launcher, the total velocity increment is obtained through the cumulative effect of each sub-rocket, expressed as

$$\Delta V_{\text{vehicle}} = \sum_{j=1}^{N} c_j \cdot \ln \left(\frac{m_0}{m_f} \right)_j \tag{2.32}$$

which can be reformulated using the payload fraction and structural coefficient:

$$\Delta V_{\text{vehicle}} = - \sum_{j=1}^{N} c_j \cdot \ln \left[\lambda_j + \varepsilon_j \left(1 - \lambda_j \right) \right] \tag{2.33}$$

The equation (2.33) indicates that the ΔV of a multistage launch vehicle varies according to the characteristics of each stage. This diversification allows for the optimisation of launch phases through the appropriate arrangement of the various stages.

There are two possible staging design configurations that can be employed: the series or parallel. In the first case, the stages are stacked one on top of the other, and ignited sequentially during the entire ascent. In the second case, lateral boosters are utilised in conjunction with the main stage during the initial phase of the flight. Both methods are utilised in launch schemes, with the configuration varying in accordance with the mission requirements, specifically in terms of $\Delta V_{mission}$, and the properties of each stage, in terms of c_j and λ_j. In practical terms, no more than four stages are used, as the gain in payload would be minimal compared to the increase in system complexity, as shown in Figure 2.8. Further details on staging can be found in various studies which also address the optimisation of each stage [13, 14].

In the current study, a strategy similar to that adopted by the Falcon 9 has been proposed. This involves two stages operating in distinct phases. The first stage focuses on initial lift-off and atmospheric ascent, while the second stage is responsible for achieving orbital insertion. The requisite values for the Falcon 9's performance parameters, including thrust, specific impulse, and structural characteristics, were obtained from the official SpaceX website [5].
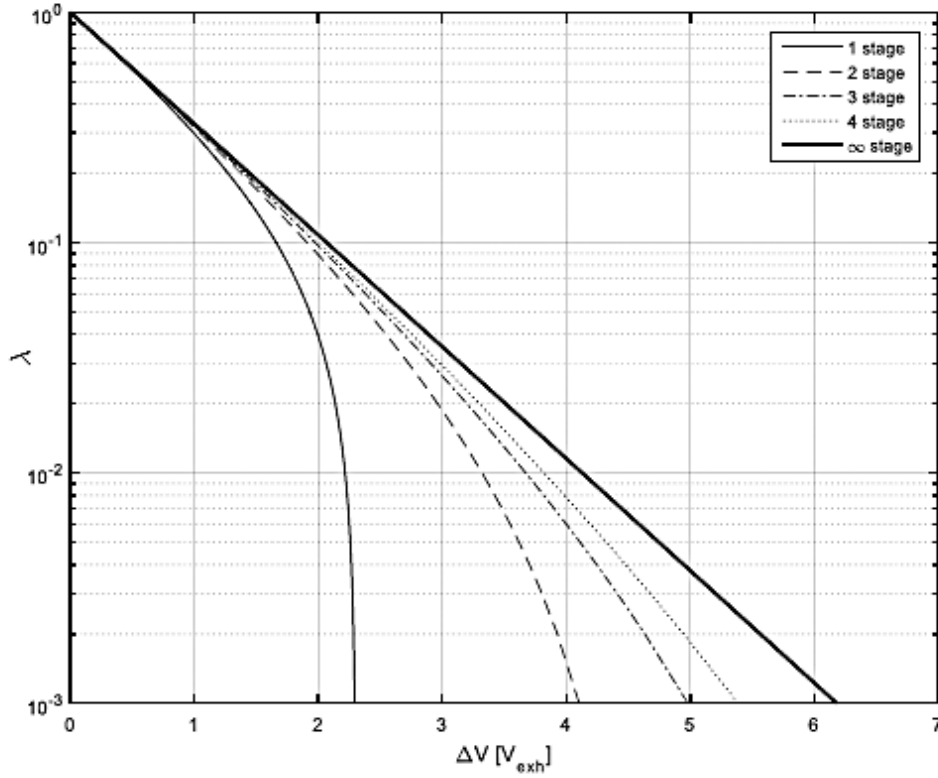
Fig. 2.8 Payload fraction dependent upon the number of stages and the requested speed

2.4   Sun-Synchronous Orbit

In the dynamic model, it is crucial to emphasise the fundamental principles underlying the definition of a SSO. As discussed in the Chapter 1 and extensively covered in the article [15], SSOs are a specific type of orbit that have gained increasing importance over time due to their characteristics, which can meet key mission requirements. These orbits are nearly polar, with inclinations ranging from 96.5 deg to 102.5 deg. As a result, they are capable of providing global coverage at all latitudes. Another noteworthy aspect of these orbits is that the line of nodes does not remain fixed but instead rotates at a rate described by the

$$\dot{\Omega} = -\frac{3}{2}J_2 \left(\frac{R_\oplus^2}{a^2} \right) \frac{\cos i}{(1 - e^2)^2} \sqrt{\frac{\mu_\oplus}{a^3}} \qquad (2.34)$$

27

As demonstrated by equation (2.34), SSOs utilise the J_2 effect, which arises due to the non-sphericity of the Earth. The bulge in the equatorial region induces an out-of-plain gravitational force, resulting in the gyroscopic precession of the orbit. Moreover, the equation demonstrates that the precession is dependent upon the orbital parameters, thereby allowing for the definition of an orbit that maintains a fixed geometry relative to the Sun. This implies that the passage of the AN can be precisely selected, allowing the SC to pass over a specific location on Earth at the same local time. Consequently, SSOs ensure that observation points along the ground track are viewed under consistent lighting conditions, which vary depending on the chosen configuration, as illustrated in Figure 2.9. This characteristic facilitates the comparison of acquired data, rendering SSOs particularly suitable for Earth observation missions, climate studies, and meteorology.
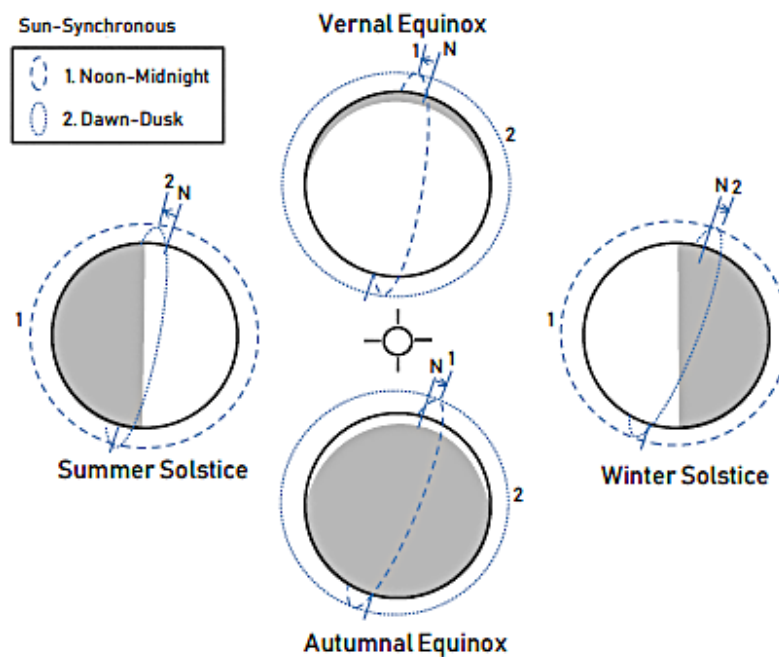
Fig. 2.9 Evolution of an SSO over time in two specific configurations

The selection of orbital parameters defining a SSO is not straightforward and is closely tied to the mission's objectives, which determine the design requirements and constraints. These orbits are employed for monitoring specific areas and, therefore, it is essential to understand the relationship between orbital precession and longitude variation.

This relationship is expressed by the equation:

$$\Delta L = (\dot{\omega}_\oplus - \dot{\Omega}) \cdot \tau_{NL}, \tag{2.35}$$

where τ_{NL} is the nodal period. In order to ensure that the satellite's coverage is confined to a particular area, it is necessary to impose that $\dot{\omega}_\oplus = \dot{\Omega}$ allows the line of nodes to rotate with the same angular velocity as the Earth's rotation around the Sun. Consequently, once Ω is fixed, the orbital parameters must be appropriately selected. Given their interdependent nature, selecting one parameter will inevitably influence the others, ensuring that mission objectives are met.

Another parameter worthy of consideration is the Mean Local Time of Ascending Node (MLTAN), which is the angle between the line of nodes and the Earth-Sun line. This allows the position of the orbital plane relative to the Greenwich meridian to be expressed in terms of relative time. If the rate of precession of an orbit matches the rate of rotation of the Earth, it becomes possible to ensure the previously mentioned lighting conditions along the entire orbit and determine the exact moment when the satellite will pass through the AN. This is exemplified by the case of 1.30 a.m. at the AN, which corresponds to an MLTAN of 22.5 deg, as shown in Figure 2.10.
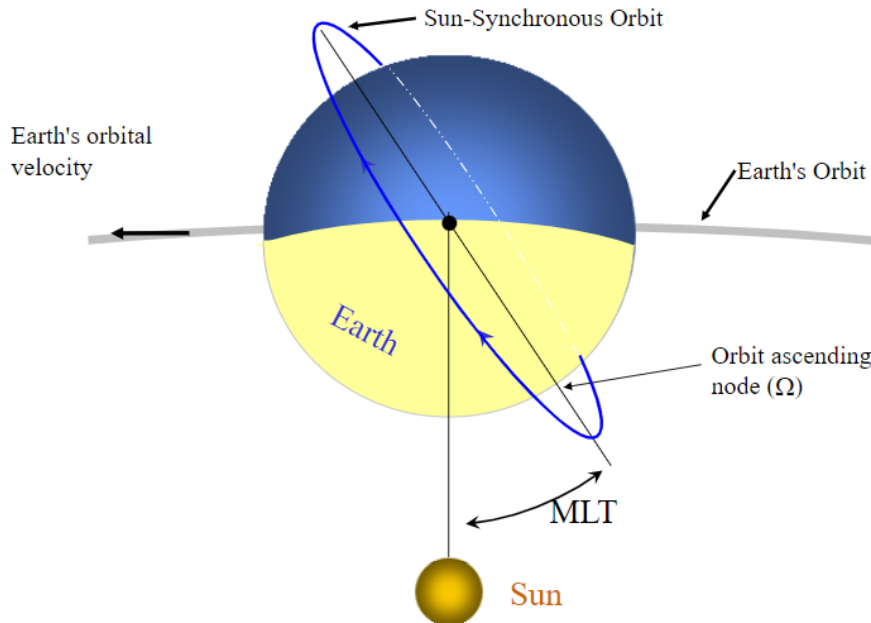
Fig. 2.10 Graphical representation of the Mean Local Time of Ascending Node

If a change in latitude is required, resulting in a shift in the observation zone, or when the timing of the AN passage necessitates adjustment, the orbital parameters may be modified to adjust the value of $\dot{\Omega}$. For a more detailed examination of the construction of SSO during the preliminary mission phases, Boain's article can be used as a reference, which has provided the foundation for this discussion [16].

2.5 Atmospheric drag

During the entire ascent phase, the launcher operates within the densest layers of the atmosphere. In light of this, the dynamic model incorporates, in addition to the perturbations resulting from the two-body interaction, the perturbative effects induced by aerodynamic drag, thereby providing a more comprehensive representation of the system's behaviour. This force, being opposite to the forward motion of the launcher, causes a deceleration that can be quantified by the following relation:

$$\boldsymbol{a}_D = -\frac{1}{2} c_D \, \rho \, \frac{S}{m} \, ||\boldsymbol{v}_{rel}|| \, \boldsymbol{v}_{rel}, \tag{2.36}$$

where the velocity is evaluated relative to the Earth's motion

$$\boldsymbol{v}_{rel}(t) = \boldsymbol{v}(t) - \boldsymbol{\omega}_E \times \boldsymbol{r}(t), \tag{2.37}$$

The drag equation (2.36) highlights that this force is contingent upon the properties of the launch vehicle, specifically its aerodynamic reference area, mass, and drag coefficient. The latter is a function of the shape and size of the launch vehicle and varies with the Mach number, an important dimensionless aerodynamic parameter that describes the flow regime of a body relative to the speed of sound, expressed as

$$M = \frac{v_{rel}}{\sqrt{\gamma \, R \, T}}. \tag{2.38}$$

The drag perturbation is directly proportional to the atmospheric density, which varies according to the altitude being considered. Given that the ascent is being modelled, the launch vehicle operates from the lower layers of the atmosphere up to the upper layers, with the dynamic system in question incorporating two different density models. The first is the exponential model, which is valid up to the stratosphere (50 km) while the second is the Harris-Priester model, which is valid

up to the thermosphere (500 km) [17]. The justification for implementing these two models lies in the fact that the former better approximates the density profile at low altitudes, following an exponential trend

$$\rho(h) = \rho_{sl}\, e^{-\frac{h}{H}}, \tag{2.39}$$

within H is a density factor of scale. In contrast, the second model demonstrates a more accurate representation of density variation at elevated altitudes. While it exhibits some limitations, such as discontinuities in the solution, it offers more precise estimates. This model accounts for the influence of latitude and diurnal variation. In the traditional Harris-Priester model, the complete expression for density is given by

$$\rho(h) = \rho_m(h) + [\rho_M(h) - \rho_m(h)]\, \cos^n\left(\frac{\Psi}{2}\right). \tag{2.40}$$

The minimum and maximum densities are calculated as

$$\rho_m(h) = \rho_m(h_i)\exp\left(\frac{h_i - h}{H_m}\right), \qquad h_i \le h \le h_{i+1} \tag{2.41a}$$

$$\rho_M(h) = \rho_M(h_i)\exp\left(\frac{h_i - h}{H_M}\right), \qquad h_i \le h \le h_{i+1} \tag{2.41b}$$

where h_i, $\rho_m(h_i)$ and $\rho_M(h_i)$ are pre-tabulated values. The exponent n varies from 2 for equatorial orbits to 6 for polar orbits, accounting for latitudinal variations in density. Scale heights are calculated using exponential interpolation to ensure continuity when transitioning between different altitudes

$$H_{m_i} = \frac{h_i - h_{i+1}}{\ln\left(\frac{\rho_m(h_{i+1})}{\rho_m(h_i)}\right)} \tag{2.42a}$$

$$H_{M_i} = \frac{h_i - h_{i+1}}{\ln\left(\frac{\rho_M(h_{i+1})}{\rho_M(h_i)}\right)}. \tag{2.42b}$$

The sinusoidal term, which accounts for diurnal density variations and depends on the position of the Sun, can be rewritten as

$$\cos^n\left(\frac{\Psi}{2}\right) = \left(\frac{1}{2} + \frac{\mathbf{r}^T \mathbf{u}_b}{2r}\right)^{\frac{n}{2}}, \tag{2.43}$$

where r is the position of the SC and $\boldsymbol{u}_b$ is a unit vector describing the relative position of the Sun, both in an ECI RF. The Sun vector $\boldsymbol{u}_b$ is expressed in terms of right ascension α_S and declination δ_S, as illustrated in the following formula

$$\mathbf{u}_b = \begin{pmatrix} \cos(\delta_s)\cos(\alpha_s + \lambda_{\text{lag}}) \\ \cos(\delta_s)\sin(\alpha_s + \lambda_{\text{lag}}) \\ \sin(\delta_s) \end{pmatrix}, \tag{2.44}$$

with λ_{lag} assumed to be 30 deg.

Consequently, the implemented atmospheric density model has a considerable impact on the drag, which is of particular significance at low altitudes but tends to diminish and become negligible at approximately 1000 km above the Earth's surface. Therefore, it might be considered that providing large at higher altitudes where drag effects are less intense would be beneficial; however, this is in opposition to gravity losses, which increase with altitude.

This thesis presents two models that have been meticulously implemented to simulate the ascent trajectory of a launch vehicle. These models incorporate variations induced by solar activity, thereby enabling a detailed examination of how different launch dates affect the vehicle's ascent. This comprehensive approach ensures a higher fidelity to real-world conditions, thereby providing valuable insights into the dynamic and complex nature of launch vehicle trajectories. By accounting for the solar activity's impact, the models offer a robust framework for optimising launch schedules and enhancing mission success rates.

Chapter 3

Optimal Control Theory

The following chapter examines the fundamental mathematical and numerical tools and concepts for analysing and solving optimisation problems typical of space missions that employ finite thrusts. The most effective approach to addressing these challenges involves the application of the Continuous-Time Optimal Control Problem (OCP).

Optimal Control Theory (OCT) is a pivotal field within engineering and applied mathematics. OCT employs mathematical methods to enhance the functionality of dynamic systems while adhering to specific constraints and objectives. Its origins lie in Calculus of Variations (CoV), a mathematical technique developed by Bernoulli in the 17th century and further developed by Euler and Lagrange in the 18th century [18]. This technique has led to the introduction of several key concepts and tools within the field of OCT, such as the Euler-Lagrange Equation. These concepts remain essential to numerous approaches in OCT in the present day, providing a framework for the identification of optimal solutions to control problems. In the early 1950s, Lev Pontryagin introduced the Maximum Principle [19], an innovative approach based on Hamilton's equations to determine the optimal control strategy, outlining the essential conditions for optimality. At the same time, Bellman developed the concept of Dynamic Programming [20], a method that involves breaking down the problem into smaller sub-problems and storing partial solutions. These two approaches laid the groundwork for the development of versatile methodological principles suited to a wide range of complexities. In recent years, OCT has expanded its scope

thanks to the advent of more powerful computing resources, thereby facilitating the development of increasingly broad and effective applications.

The core principle of OCT is to identify a control law that optimises an objective function, typically defined in terms of cost or efficiency, over a specified time period. This optimisation process is based on the analysis of the system dynamics, which are described using differential equations or finite differences, and their interaction with adjustable variables. The focus is on finding optimal solutions, selecting them from many sub-optimal alternatives, even in complex contexts with stringent constraints. This process employs dynamic programming algorithms and non-linear programming techniques.

A key illustration of the application of this theory can be observed in the definition of optimal ascent trajectories, which are designed to enhance the performance of an aerospace vehicle during the critical launch phase. The primary goal is to minimize or maximize an objective function, typically associated with variables such as fuel consumption, flight time, or maximum payload. A fundamental aspect of this process is the continuous monitoring of specific parameters throughout the entirety of the trajectory. This allows for the determination of the ideal temporal evolution of variables that comply with constraints and maximize efficiency. The optimal control variables are grouped under the term *"optimal control laws"*, which are essential for distinguishing the optimal solution from other possibilities.

The third chapter is structured as follows. The initial section of the chapter delineates the distinction between two numerical methodologies applicable to OCP: Direct Methods and Indirect Methods. This section will also present the rationale for the preference of Indirect Methods over Direct ones. Subsequently, the second paragraph examines a typical OCP as a Two-Point Boundary Value Problem (TPBVP), discussing the results obtained and the conditions of optimality. In the third paragraph, the discussion extends to a Multi-Point Boundary Value Problem (MPBVP), illustrating the resolution process through the single shooting method. Finally, the chapter will examine how OCT can be employed with a view to optimise ascent trajectories. In particular, it will investigate the Hamiltonian boundary value problem (HBVP), utilising a medium-fidelity approach in order to achieve accurate results.

3.1   A comparison of Direct and Indirect Methods

A numerical method is a mathematical strategy employed to address problems that are challenging to resolve with precise analytical techniques, frequently due to the complexity of the involved equations. The objective of this approach is to decompose a complex problem into a series of smaller, more manageable problems. This process, known as *problem transcription*, is focused on a specific case study. The main idea is to transform sets of differential equations, which represent phenomena that are continuous in time or space, into discrete systems composed of a limited number of points, defined as *intervals*, based on a reduced number of variables. The optimization problem of trajectories under examination is continuous over time, but it can be reconfigured using numerical methods to convert it from an infinite-dimensional problem into a series of finite-dimensional sub-problems. Numerical methods are mainly divided into two categories: Direct (DM) and Indirect (IM).

The selection of an appropriate method has historically been a source of disagreement among academics. Traditionally, DMs have been favoured due to their robustness, ease of implementation, and ability to address complex issues, resulting in definitive solutions without the need for further iterations. However, they also present disadvantages, such as potential imprecision and high computational costs due to the need to manage a dense domain with many critical points, known as nodes. Currently, challenges related to computational costs have been mitigated by the use of more advanced computers.

On the other hand, IMs provide highly accurate solutions with a lower computational cost. These methods begin with an approximate solution and, through subsequent iterations, guide toward the final solution until a predetermined convergence criterion is met. This approach not only aids in understanding the problem but also offers insights on how to enhance the solution towards optimality. Despite their advantages, IMs may face challenges with convergence, which is not guaranteed in all cases and depends on the initial conditions and characteristics of the system. Moreover, the resolution of an OCP through these methodologies necessitates the construction of a specific model and the manual calculation of requisite parameters. Further detailed discussion on these methodologies can be found in Betts's work [21].

The present study focuses on the utilisation of IMs for trajectory optimisation. This approach has garnered significant support from the scientific community over the years. A multitude of research and publications, including those developed within the Politecnico di Torino [22, 23], have highlighted the great flexibility and adaptability of these methods to a wide range of engineering problems, such as the optimization of space trajectories. A central element of these studies is the strategic management of intervals to effectively handle constraints and discontinuities, transitioning from a TPBVP to a MPBVP. The adoption of sophisticated numerical techniques has substantially improved the robustness of IMs, thereby enhancing their suitability for resolving more intricate challenges.

For the aforementioned reasons, this thesis implements an algorithm that utilises indirect methods to optimise ascent trajectories. This approach is chosen for its versatility and reliability, making it an effective computational tool that is capable of finding optimal solutions for the problem under study.

3.2 Optimal Control Theory

As already mentioned, a crucial element in OCT is the selection of a suitable control strategy that facilitates the transition from the initial state to the final state of the dynamic system under analysis. In this process, it is essential to ensure that all constraints are respected and that the optimisation criterion is aimed at maximising (or minimising) the merit index.

For the OCP, it is essential to define a control model that accurately describes the system dynamics. In this study, the control system is characterized using a set of Ordinary Differential Equations (ODEs). These ODEs can generally be expressed as follows

$$\dot{\boldsymbol{x}}(t) = \boldsymbol{f}(\boldsymbol{x}(t), \boldsymbol{u}(t), t) \tag{3.1}$$

Therefore, the OCP consists of a set of first-order ODE ($\dot{\boldsymbol{x}}$) that describe how the n-state variables evolve over time. These ODEs are function of a state vector, $x(t) \in \mathbb{R}^n$, which fully defines the characteristics of the system of interest, and a control vector, $u(t) \in \mathbb{R}^m$, which consists of m-control variables. Both vectors are functions of the time between the initial and final instants. In addition, time is considered as an independent variable. Consequently, to obtain an optimal solution,

it is necessary to identify an optimal trajectory, $x^*(t)$, managed by an optimal control, $u^*(t)$, that maximises the merit index.

In general, a trajectory depends on the conditions established at the initial and final moments, denoted t_0 and t_f respectively, which serve as Boundary Condition (BC) for a TPBVP. The optimal trajectory needs to satisfy several constraints. If these constraints only concern the state and the time at the end points of the trajectory, they can be formulated as a set of homogeneous, typically non-linear, algebraic equations. The BCs can be organised into a constraint vector as follows

$$\boldsymbol{\chi}\left(\boldsymbol{x}_0,\boldsymbol{x}_f,t_0,t_f\right) = \boldsymbol{0} \tag{3.2}$$

where $\boldsymbol{\chi} : [\mathbb{R}^n, \mathbb{R}^n, \mathbb{R}, \mathbb{R}] \to \mathbb{R}^q$ which contains all q different constraints.

The optimality pattern for an OCP can be defined by an objective function, or merit index, denoted $\mathcal{J}$. In this context, points x within the domain for which the first derivative $f'(x) = 0$ are identified as *extremum* points of the function f. Thus, it is necessary to evaluate the extremal values corresponding to the maximum (or minimum) points. The merit index can then be written as

$$\mathcal{J} = \varphi(\boldsymbol{x_0},\boldsymbol{x_f},t_0,t_f) + \int_{t_0}^{t_f} \left[\boldsymbol{\Phi}(\boldsymbol{x}(t),\boldsymbol{u}(t),t)\right] dt. \tag{3.3}$$

Two main scalar components arise from the merit index $\mathcal{J}$ (3.3). The first function (φ) is dependent on the values assumed by the variables and the times at the extreme limits, and thus depends on the specific admissible final state obtained among the various ones sought. Meanwhile, the integral of the second function (Φ) is determined by the values that the state variables, controls, and time itself take over the considered interval, thereby quantifying the solution's evolution from the initial to the final state. The aforementioned issue, outlined in equations (3.1) to (3.3), is known as Bolza problem [24], which represents a classic example of the CoV OCP. The objective of this problem is to optimise a time-continuous set of ODEs, while satisfying the specified BCs.

With the introduction of auxiliary variables, the functional $\mathcal{J}$ can be reformulated into two different expressions: the first is the Lagrange form, obtained by setting $\varphi = 0$, and the second is the Mayer form, achieved with $\Phi = 0$. Among these, the Mayer formulation is the most commonly used, as it not only simplifies the problem

formulation but also facilitates the derivation of first-order analytical conditions in a more direct manner.

The principles of IMs are now implemented, and significant manipulations are carried out. The optimality conditions are determined by the introduction of an augmented merit function, $\mathcal{J}^*$, which incorporates a measure of how well constraints and state quantities, in relation to the ODEs of the evolving dynamic model, are adhered to. For this process, additional variables, also known as *co-state variables*, will be introduced. Such variables are collected in the adjoint vector, $\lambda(t) \in \mathbb{R}^n$, which is associated with the state variables of the problem. Concurrently, the Lagrange multipliers are incorporated into the vector $\mu \in \mathbb{R}^m$, which is linked to the BCs. Consequently, the augmented merit index assumes a specific form

$$\mathcal{J}^* = \varphi + \mu^T \chi + \int_0^{t_f} \left[\Phi + \lambda^T (f - \dot{x}) \right] dt. \tag{3.4}$$

Both functional in equations (3.3) and (3.4) are closely linked to the state variables $x(t)$, their derivatives $\dot{x}(t)$, and the control vector $u(t)$. It should be noted that in the case of a non-converging solution, where $\chi \neq 0$, the equation (3.3) is not satisfied, resulting $f \neq \dot{x}$. However, if both the BCs and state equations are respected, then $\chi = 0$, $f = \dot{x}$, and consequently $\mathcal{J} = \mathcal{J}^*$. Therefore, solving the augmented problem posed by the merit index in equation (3.4) is mathematically equivalent to solving the problem in equation (3.3), once all constraints have been fulfilled.

In the equation (3.4), the presence of time derivatives of state variables is observed, which are integrated during the trajectory optimisation process. Since these terms are ideally unknown, it is necessary to eliminate them by integration $(-\lambda^T \dot{x})$ term by parts

$$\int_0^{t_f} \left(-\lambda^T \dot{x} \right) dt = - \left(\lambda_f^T x_f \right) + \left(\lambda_0^T x_0 \right) + \int_0^{t_f} \left(\dot{\lambda}^T x \right) dt \tag{3.5}$$

Therefore, by combining the equations (3.5) and (3.4), one can write

$$\mathcal{J}^* = \varphi + \mu^T x + \left(\lambda_0^T x_0 - \lambda_f^T x_f \right) + \int_0^{t_f} \left(\Phi + \lambda^T f - \dot{\lambda}^T x \right) dt \tag{3.6}$$

38

A term of considerable significance has emerged within the equation (3.6), namely the system's Hamiltonian

$$\mathcal{H} \triangleq \mathbf{\Phi} + \boldsymbol{\lambda}^T \boldsymbol{f} \tag{3.7}$$

The merit index $\mathcal{J}^*$ can be maximised (or minimised) only if the essential condition of optimality is met. This condition requires that $\mathcal{J}^*$ be stationary at the optimal point. This means that the first-order variation of $\mathcal{J}^*$ must be zero. The first-order differentiation, $\delta \mathcal{J}^*$, can be derived through several mathematical steps

$$\delta \mathcal{J}^* = \left(\frac{\partial \varphi}{\partial t_0} + \boldsymbol{\mu}^T \frac{\partial \boldsymbol{\chi}}{\partial t_0} - \mathcal{H}_0 \right) \delta t_0 + \tag{3.8a}$$

$$+ \left(\frac{\partial \varphi}{\partial t_f} + \boldsymbol{\mu}^T \frac{\partial \boldsymbol{\chi}}{\partial t_f} + \mathcal{H}_f \right) \delta t_f + \tag{3.8b}$$

$$+ \left(\frac{\partial \varphi}{\partial \boldsymbol{x}_0} + \boldsymbol{\mu}^T \frac{\partial \boldsymbol{\chi}}{\partial \boldsymbol{x}_0} + \boldsymbol{\lambda}_0^T \right) \delta \boldsymbol{x}_0 + \tag{3.8c}$$

$$+ \left(\frac{\partial \varphi}{\partial \boldsymbol{x}_f} + \boldsymbol{\mu}^T \frac{\partial \boldsymbol{\chi}}{\partial \boldsymbol{x}_f} - \boldsymbol{\lambda}_f^T \right) \delta \boldsymbol{x}_f + \tag{3.8d}$$

$$+ \int_{t_0}^{t_f} \left[\left(\frac{\partial \mathcal{H}}{\partial \boldsymbol{x}} + \dot{\boldsymbol{\lambda}}^T \right) \delta \boldsymbol{x} + \frac{\partial \mathcal{H}}{\partial \boldsymbol{u}} \delta \boldsymbol{u} \right] dt, \qquad j = 1, \dots, n_p. \tag{3.8e}$$

A suitable selection of adjoint variables $\boldsymbol{\lambda}$ and Lagrange multipliers $\boldsymbol{\mu}$ can effectively make $\delta \mathcal{J}^*$ equal to zero for any variations $\delta t_0, \delta t_f, \delta \boldsymbol{x}_0, \delta \boldsymbol{x}_f, \delta \boldsymbol{x}$, and $\delta \boldsymbol{u}$, by eliminating their corresponding multiplying coefficients. Each specific part of equation (3.8) leads to different sets of conditions. In particular, when the coefficient multipliers in equations (3.8a) and (3.8b) are zero, a pair of algebraic equations known as the *transversality conditions* is presented at the start and end times, respectively. In contrast, equations (3.8c) and (3.8d) produce $2n$ algebraic equations, corresponding to each state variable at both the initial and final boundaries, which are known as *optimality conditions*. Finally, the two farther multiplying coefficients generate two key outcomes: n Euler-Lagrange ODEs for the adjoint variables and m algebraic equations for the control.

3.2.1 Boundary Conditions for Optimal Solution

The boundary conditions for achieving optimality consist of a set of ODEs that regulate the behaviour of times (2 transversality conditions) and states ($2n$ optimality conditions) at the extremities of the trajectory. By setting the multiplying coefficients $(\delta t_0, \delta t_f, \delta \boldsymbol{x}_0, \delta \boldsymbol{x}_f)$ in equation (3.8) to zero, one can readily derive the following results

$$\frac{\partial \varphi}{\partial t_0} + \boldsymbol{\mu}^T \frac{\partial \boldsymbol{\chi}}{\partial t_0} - \mathcal{H}_0 = 0 \tag{3.9a}$$

$$\frac{\partial \varphi}{\partial t_f} + \boldsymbol{\mu}^T \frac{\partial \boldsymbol{\chi}}{\partial t_f} + \mathcal{H}_f = 0 \tag{3.9b}$$

$$\frac{\partial \varphi}{\partial \boldsymbol{x}_0} + \boldsymbol{\mu}^T \frac{\partial \boldsymbol{\chi}}{\partial \boldsymbol{x}_0} - \boldsymbol{\lambda}_0^T = \boldsymbol{0} \tag{3.9c}$$

$$\frac{\partial \varphi}{\partial \boldsymbol{x}_f} + \boldsymbol{\mu}^T \frac{\partial \boldsymbol{\chi}}{\partial \boldsymbol{x}_f} + \boldsymbol{\lambda}_f^T = \boldsymbol{0} \tag{3.9d}$$

A series of considerations can be made in relation to the aforementioned equations. Considering the first two transversality equations, (3.9a) and (3.9b), the Hamiltonian is identically zero at that point at both initial and final times, if time is not present in the function φ and is unconstrained, and the time values are determined by the optimisation process. Conversely, the Hamiltonian is unconstrained and assumes a specific value if time is constrained, i.e., if constraints such as $t_0 = a$ and/or $t_f = b$ exist in $\boldsymbol{\chi}$. To illustrate this key concept, consider a space mission with a fixed duration Δt, where the initial moment t_0 and the final moment $t_f = t_0 + \Delta t$ are known; in this scenario, both $\mathcal{H}_0$ and $\mathcal{H}_f$ are non-null. On the other hand, in a mission where the value of t_f is not fixed, it becomes the subject of the optimization, resulting in $\mathcal{H}_f = 0$ while $\mathcal{H}_0 \neq 0$, since t_0 is known.

Similarly, the optimality conditions of equations (3.9c) and (3.9d) dictate that if a generic *i-th* state variable (x_i) does not appear in either the function φ or any constraint, then the corresponding added variable λ_{x_i} will be zero at the same point. Conversely, if the variable state x_i is assigned, the corresponding added variable will be free, thus $\lambda_{x_i} \neq 0$.

3.2.2 Adjoint and Control variables equations

The last line (3.8e) of Equation (3.8) will result in a set of ODEs by nullifying their respective multiplicative coefficients. These equations enable the description of how the augmented variables and controls evolve over time. In expression (3.8e), it is possible to proceed by setting two terms to zero, namely $\delta\boldsymbol{x}$ and $\delta\boldsymbol{u}$.

By nullifying the coefficient $\delta\boldsymbol{x}$, one obtains the Euler-Lagrange equations for the adjoint variables

$$\frac{d\boldsymbol{\lambda}}{dt} = -\left(\frac{\partial \mathcal{H}}{\partial \boldsymbol{x}}\right)^T. \tag{3.10}$$

As the adjoint variables are closely related to the state variables, it follows that $\dot{\lambda} \in \mathbb{R}^n$. If the coefficient $\delta\boldsymbol{u}$ is nullified, a set of m algebraic equations for control will be obtained, precisely

$$\left(\frac{\partial \mathcal{H}}{\partial \boldsymbol{u}}\right)^T = 0. \tag{3.11}$$

In the most basic terms, it can be stated that some elements of the control vector $\boldsymbol{u}$ may be required to adhere to specific limits of admissibility, namely $\mathcal{U}$. Typically, the control vector $\boldsymbol{u}$ is influenced by the state variables and the time, represented as $\boldsymbol{u}(\boldsymbol{x}(t), t)$. In the current context, only explicit constraints are taken into account. For instance, a specific control variable $\boldsymbol{u}$ ought to be maintained within the boundaries $\mathcal{U}_{min} \le \boldsymbol{u} \le \mathcal{U}_{max}$. Given explicit admissibility constraints, the optimal control $\boldsymbol{u}^* \in \mathcal{U}$ for the target trajectory is determined by finding those values that extremizes the Hamiltonian at each point of the trajectory, as specified in Equation (3.7). This approach is based on Pontryagin's Maximum Principle (PMP) for problems involving maximisation, or Pontryagin's Minimum Principle (PmP) for those requiring minimisation [19]. The PMP does not necessarily require that a control be limited to the extreme values within its allowable range. The optimal control value is typically determined according to Equation (3.11) provided that $\mathcal{U}_{min} \le \boldsymbol{u} \le \mathcal{U}_{max}$, making it unconstrained. If this condition is not met, the control value is set at the boundaries of $\mathcal{U}$.

Nevertheless, Equation (3.11) is not applicable in the case of a linear or affine Hamiltonian, as described in Equation (3.7), in terms of the bounded control. In

such a case, two distinct scenarios emerge

$$\frac{\partial \mathcal{H}}{\partial u_i} = \begin{cases} k_{u_i} & \text{constant, if } \mathcal{H} \text{ affine wrt } u_i \\ f(u_i) & \text{otherwise} \end{cases} \tag{3.12}$$

In case of the Hamiltonian being affine to the control, it is generally not possible to satisfy equation (3.12) unless $k_{u_i} = 0$, because u_i should not explicitly influence the outcome. In such circumstances, the approach to be taken depends on the value of the coefficient k_{u_i} derived from the equation. To maximize the Hamiltonian, the control u_i must be adjusted in accordance with the specific sign of k_{u_i}, if not null. If $k_{u_i} > 0$ the optimal strategy involves setting u_i to its highest permissible value, specifically $u_i = \mathcal{U}_{i,max}$. On the other hand, when $k_{u_i} < 0$, the optimal involves setting u_i to its minimum allowable value, $u_i = \mathcal{U}_{i,min}$.

The phenomenon under discussion is referred to as *bang-bang control*, which precisely characterises the situation presented in the OCP being considered. In this context, the Hamiltonian demonstrates a linear relationship with the control variable, specifically the angle, based on certain assumptions that will be detailed in the following chapter. Furthermore, the decision to switch between the two extreme values, namely the minimum and maximum, is critical in determining the optimal trajectory. Should the control variable k_{u_i} equals zero over a specific time period, an alternative strategy must be explored. This operation, as described in [25], involves the presence of singular arcs, which will not be addressed in this thesis as they are not of interest.

A TPBVP is presented, characterised by m-constraint conditions $\chi = 0$, described by two transversality equations, (3.9a) and (3.9b), $2n$ optimality equations, (3.9c) and (3.9d), and m-control equations (3.11). This set of equations implicitly determines the initial and final times, t_0 and t_f, the initial state values for the $2n$ ODEs, for x and λ, and m-adjoint constants, μ.

3.3   Multi-Point Optimal Control Problem

The concept of MPBVP is introduced when internal conditions are applied along the trajectory, i.e., varying thrust conditions to execute launcher staging for orbital ascent.

This strategy involves the division of the trajectory into a number of sub-intervals, n_p, which are commonly referred to as *arcs*. This division enhances the robustness and facilitates convergence of the code. In this implementation, the problem outlined in Equations (3.1) to (3.3) is transformed into a MPBVP. Each j-th arc begins at $t_{(j-1)_+}$ and ends at t_{j_-}, with extremal state variable vectors denoted as $\boldsymbol{x}_{(j-1)_+}$ and $\boldsymbol{x}_{j_-}$, respectively. It is worth noting that each variable is continuous within each arc. However, it is important to be aware that discontinuities do occur at the internal boundaries, namely at the points connecting two arcs.

Figure 3.1 provides a schematic representation of a generic MPBVP, where an abbreviated notation $\left(\boldsymbol{x}(t_j) \triangleq \boldsymbol{x}_j\right)$ is introduced for simplicity.
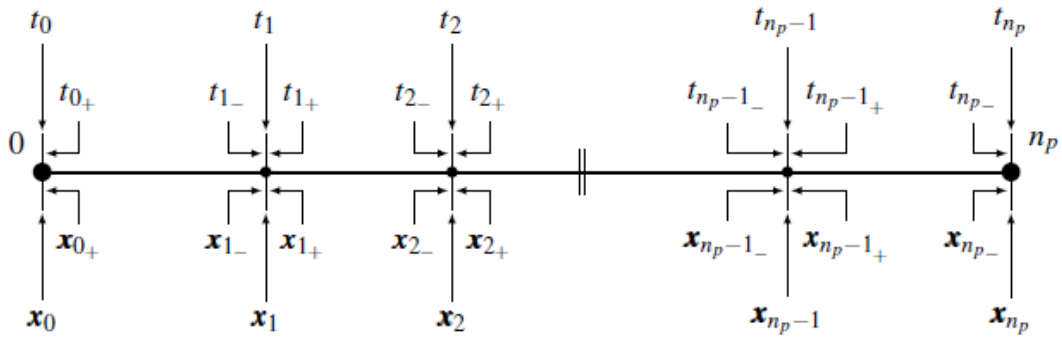
Fig. 3.1 Multipoint Boundary Value Problem diagram composed by n_p arcs, [9]

As previously mentioned, BCs are generally non-linear and mixed. In a MPBVP, the aforementioned conditions can be imposed both internally and externally to the boundaries, as illustrated in equation (3.2). These may be influenced by both state variables and the independent time variable. Consequently, they can be reformulated in the following way

$$\boldsymbol{\chi}\left(\boldsymbol{x}_{(j-1)_+}, \boldsymbol{x}_{j_-}, t_{(j-1)_+}, t_{j_-}\right) = 0, \qquad j = 1, \ldots, n_p. \tag{3.13}$$

The functional $\mathcal{J}$ for an OC MPBVP thus becomes

$$\mathcal{J} = \varphi\left(\boldsymbol{x}_{(j-1)_+}, \boldsymbol{x}_{j_-}, t_{(j-1)_+}, t_{j_-}\right) + \sum_{j=1}^{n_p} \int_{t_{(j-1)_+}}^{t_{j_-}} \Phi\left(\boldsymbol{x}(t), \boldsymbol{u}(t), t\right) dt. \tag{3.14}$$

In the equation (3.14), the function φ is determined by the values that variables and times take at each boundary across the entire trajectory, from $j = 0$ to $j = n_p$, as well as within each individual arc. The total sum of all integrals of the function Φ are influenced by the changes over time in state variables, controls, and time itself, effectively outlining the evolution of the solution on an arc-by-arc basis. The augmented merit index J^* for the MPBVP is presented in the form

$$\mathcal{J}^* = \varphi + \boldsymbol{\mu}^T \boldsymbol{\chi} + \sum_{j=1}^{n_p} \int_{t_{(j-1)_+}}^{t_{j_-}} \left[\Phi + \boldsymbol{\lambda}^T (\boldsymbol{f} - \dot{\boldsymbol{x}}) \right] dt \tag{3.15}$$

and, by eliminating the term involving the derivative of the state variables via integration by parts

$$\mathcal{J}^* = \varphi + \boldsymbol{\mu}^T \boldsymbol{\chi} + \sum_{j=1}^{n_p} \left(\boldsymbol{\lambda}_{(j-1)_+}^T \boldsymbol{x}_{(j-1)_+} - \boldsymbol{\lambda}_{j_-}^T \boldsymbol{x}_{j_-} \right)$$
$$+ \sum_{j=1}^{n_p} \int_{t_{(j-1)_+}}^{t_{j_-}} \left(\Phi + \boldsymbol{\lambda}^T \boldsymbol{f} - \dot{\boldsymbol{\lambda}}^T \boldsymbol{x} \right) dt. \tag{3.16}$$

First order derivative of the augmented functional $\mathcal{J}^*$ is rewritten for each arc as

$$\delta \mathcal{J}^* = \left(\frac{\partial \varphi}{\partial t_{(j-1)_+}} + \boldsymbol{\mu}^T \frac{\partial \boldsymbol{\chi}}{\partial t_{(j-1)_+}} - \mathcal{H}_{(j-1)_+} \right) \delta t_{(j-1)_+} + \tag{3.17a}$$

$$+ \left(\frac{\partial \varphi}{\partial t_{j_-}} + \boldsymbol{\mu}^T \frac{\partial \boldsymbol{\chi}}{\partial t_{j_-}} + \mathcal{H}_{j_-} \right) \delta t_{j_-} + \tag{3.17b}$$

$$+ \left(\frac{\partial \varphi}{\partial \boldsymbol{x}_{(j-1)_+}} + \boldsymbol{\mu}^T \frac{\partial \boldsymbol{\chi}}{\partial \boldsymbol{x}_{(j-1)_+}} + \boldsymbol{\lambda}_{(j-1)_+}^T \right) \delta \boldsymbol{x}_{(j-1)_+} + \tag{3.17c}$$

$$+ \left(\frac{\partial \varphi}{\partial \boldsymbol{x}_{j_-}} + \boldsymbol{\mu}^T \frac{\partial \boldsymbol{\chi}}{\partial \boldsymbol{x}_{j_-}} - \boldsymbol{\lambda}_{j_-}^T \right) \delta \boldsymbol{x}_{j_-} + \tag{3.17d}$$

$$+ \sum_{j=1}^{n_p} \int_{t_{(j-1)_+}}^{t_{j_-}} \left[\left(\frac{\partial \mathcal{H}}{\partial \boldsymbol{x}} + \dot{\boldsymbol{\lambda}} \right) \delta \boldsymbol{x} + \frac{\partial \mathcal{H}}{\partial \boldsymbol{u}} \delta \boldsymbol{u} \right] dt, \qquad j = 1, \dots, n_p. \tag{3.17e}$$

In the domain of MPBVP, it is more effective to express optimality and transversality conditions directly in relation to the boundary itself. Consequently, rather than focusing solely on an individual j-th arc spanning from $t_{(j-1)_+}$ to t_{j_-}, emphasis is placed on the boundary. Values just prior to and following the boundary are then

considered for analysis.

$$\frac{\partial \varphi}{\partial t_{j_+}} + \boldsymbol{\mu}^T \frac{\partial \boldsymbol{\chi}}{\partial t_{j_+}} - \mathcal{H}_{j_+} = 0, \qquad j = 1,\ldots,n_p - 1 \qquad (3.18\text{a})$$

$$\frac{\partial \varphi}{\partial t_{j_-}} + \boldsymbol{\mu}^T \frac{\partial \boldsymbol{\chi}}{\partial t_{j_-}} + \mathcal{H}_{j_-} = 0, \qquad j = 1,\ldots,n_p \qquad (3.18\text{b})$$

$$\frac{\partial \varphi}{\partial \boldsymbol{x}_{j_+}} + \boldsymbol{\mu}^T \frac{\partial \boldsymbol{\chi}}{\partial \boldsymbol{x}_{j_+}} + \boldsymbol{\lambda}_{j_+}^T = \boldsymbol{0}, \qquad j = 1,\ldots,n_p - 1 \qquad (3.18\text{c})$$

$$\frac{\partial \varphi}{\partial \boldsymbol{x}_{j_-}} + \boldsymbol{\mu}^T \frac{\partial \boldsymbol{\chi}}{\partial \boldsymbol{x}_{j_-}} - \boldsymbol{\lambda}_{j_-}^T = \boldsymbol{0}, \qquad j = 1,\ldots,n_p. \qquad (3.18\text{d})$$

It is of interest to highlight that the Euler-Lagrange equations, both for the adjoints equations and those for the control, maintain their validity within the domain of MPBVP.

3.4 Comprehensive Implementation of Boundary Value Problem

This section sets forth the implementation of the Boundary Value Problem (BVP) in the context of OCT. The principal objective is to optimize the ascent trajectory of a launcher subject to gravitational effects within a medium-fidelity Two-Body Problem (2BP). The implementation of BVP requires the application of precise control and optimisation processes in order to address the potential numerical issues which may hinder the convergence of solutions, due to the highly non-linear nature of the problem. In light of the use of IM, particular emphasis must be placed on the robustness of the code and the high sensitivity of the solution with respect to variations in initial conditions.

To address this problem, a TPBVP is proposed. This approach is feasible because OCT extends the size of the problem compared to the original 2BP, as discussed in the previous sections. In this context, the initial state includes the original state variables, some of which may be unknown, along with an adjoint vector:

$$\boldsymbol{y}_0 = \left\{ (\boldsymbol{x})^T (\boldsymbol{\lambda})^T \right\}^T \qquad (3.19)$$

The objective of such a BVP investigated here is to determine the optimal initial conditions of the state variables, $\mathbf{y}_0^*$, that enable the desired final conditions $\mathbf{y}_f^*$ to be fulfilled. Throughout this process, it is critical to ensure that all BCs are continually satisfied, including both the constrained and the optimality conditions. The *single-shooting method* is the preferred approach for its straightforward implementation and computational demands. This methodology allows for the cyclic adjustment and updating of the initial conditions, thereby facilitating the achievement of the desired final conditions, as will be more clearly explained in this current work [9]. This approach is consistent with the goal of developing a practical solution methodology based on IM, effectively managing the dynamics of the 2BP.

Generally, the method and the full set of ODEs for an IM can be formulated as follows

$$\dot{\mathbf{y}}(t) = \mathbf{f}(\mathbf{y}(t), t) \tag{3.20}$$

By introducing a new vector $\mathbf{z} = \left\{\mathbf{y}^T \ \mathbf{c}^T\right\}^T$, which incorporates the constant vector $\mathbf{c}$, the set of ODEs can be reformulated as

$$\dot{\mathbf{z}} = \frac{d\mathbf{z}}{dt} = \mathbf{f}(\mathbf{z}(t), t), \tag{3.21}$$

with

$$\dot{\mathbf{c}} = \frac{d\mathbf{c}}{dt} = 0. \tag{3.22}$$

The newly formulated set of BCs, which includes both imposed and optimal conditions, are satisfied when it returns

$$\boldsymbol{\chi}(z) = \mathbf{0}, \tag{3.23}$$

where the vector $\mathbf{z}$ contains all the values assumed by the variables at the inner and outer boundary.

The current analysis focuses on identifying the optimal initial values for the design vector that result in the desired final conditions while maintaining adherence to all constraints. To achieve this objective, a single-shooting method is utilized to identify the most optimal initial state, $\mathbf{q}_0^*$, which fulfils the BCs, so that $\boldsymbol{\chi}(\mathbf{q}^*) = 0$. The following notation $\boldsymbol{\chi}(\mathbf{q}_r) \triangleq \boldsymbol{\chi}_r$ is taken into account for the deviation of the BCs at each r-th iteration. The iterative process starts with the assumption of $\mathbf{q}_r = \mathbf{z}_0$ as initial vector for the variables, all of which are considered unknown. In subsequent

iterations, the BCs are updated based on the values of the BCs and state vector from the previous iteration. This relationship is modelled using a first-order Taylor expansion, where the Jacobian matrix, denoted by $\mathcal{J}(\boldsymbol{\chi}_r) \triangleq \mathcal{J}\left(\boldsymbol{\chi}(\boldsymbol{q}_r), \boldsymbol{q}_{r+1}\right)$, is formed by the partial derivatives of the constraint vector with respect to the forward-in-time free-variable vector quantities

$$\boldsymbol{\chi}(\boldsymbol{q}_{r+1}) = \boldsymbol{\chi}(\boldsymbol{q}_r) + \frac{\partial \boldsymbol{\chi}(\boldsymbol{q}_r)}{\partial \boldsymbol{q}_{r+1}}(\boldsymbol{q}_{r+1} - \boldsymbol{q}_r). \tag{3.24}$$

In the event that a solution exists, then $\boldsymbol{\chi}_{r+1} = 0$, and the iterative solution takes the following form

$$\boldsymbol{\chi}_r + [\mathcal{J}(\boldsymbol{\chi}_r)]\left(\boldsymbol{q}_{r+1} - \boldsymbol{q}_r\right) = 0. \tag{3.25}$$

Consequently, at each iteration, it is possible to calculate the state of the design vector $\boldsymbol{z}_r$ and update the value of the constraint vector $\boldsymbol{\chi}_r$

$$\boldsymbol{q}_{r+1} = \boldsymbol{q}_r - [\mathcal{J}(\boldsymbol{\chi}_r)]^{-1}\boldsymbol{\chi}_r. \tag{3.26}$$

In this context, the Jacobian matrix is calculated as follows

$$\mathcal{J}(\boldsymbol{\chi}_r) = \frac{\boldsymbol{\chi}_r^p - \boldsymbol{\chi}_r}{\Delta}, \tag{3.27}$$

in which $\boldsymbol{\chi}^p$ represents the constraint vector associated with the perturbed vector $\boldsymbol{q}^p$, with the perturbation magnitude Δ is set to 1×10^{-7}. For each variable element,

$$\chi_r^p \triangleq \chi(q_r^p) \tag{3.28a}$$

$$q_r^p \triangleq q_r + \Delta. \tag{3.28b}$$

In order to compute the Jacobian matrix, a forward finite difference approach is employed, as outlined in Equation (3.27). It should be noted that this introduces a certain degree of approximation, nevertheless this methodology enhances the stability of a system that is subjected to variation in the initial conditions.

Consequently, the OCP formulated within the TPBVP aims to determine the optimal initial state $\boldsymbol{z}_0^*$ that steers the trajectory towards the desired final state $\boldsymbol{z}_f^*\left(\boldsymbol{z}_0^*(t), t\right)$, while complying with all BCs. This is achieved through the simultaneous integration of both the principal set of ODEs and all the STM equations via the lsoda integrator [26], which employs variable step sizes and orders in accordance with

Adams-Moulton methods [27]. The equations are outlined below for clarity

$$\dot{z} = f(z(t), t). \tag{3.29}$$

The implementation of linear mapping via the STM in the iterative Differential Corrector (DC) process can introduce errors that may inhibit convergence and lead to divergences. In order to enhance the robustness of this method, two principal strategies have been introduced with the purpose of managing the maximum error, which is denoted as $E_{max} = norm_i(\chi_i)$. Firstly, a correction factor is introduced in Equation (3.30) during the iterative process, which, when properly selected, ensures the convergence of the solution. This factor is also known as the relaxation parameter κ_1 and varies between 0.1 and 1. Consequently, the equation is given as:

$$z_{r+1} = z_r - \kappa_1 \cdot [\partial(\chi_r)]^{-1} \chi_r. \tag{3.30}$$

During the preliminary estimation phase, lower values of κ_1 should be used for unknown variables, while higher values are recommended once the solution is in close proximity to the optimal one. Secondly, the error in the subsequent steps is controlled by comparison with the errors in the boundary conditions of the previous step,

$$E_{max,r+1} < \kappa_2 \, E_{max,r}. \tag{3.31}$$

Values of κ_2 between 2 and 3 generally promote convergence during the initial stage of the iterative process. Although these initial steps set the optimal direction, they may also result in an increase in the maximum error. If equation (3.31) is not satisfied, a correction process will be implemented on κ_1.

3.5 OCP application for ascent optimization

In this section, the dynamics of a launch vehicle subject to optimization are presented with the aim of identifying the optimal ascent trajectory. Before proceeding, it is necessary to provide a detailed explanation of the dimensionless parameters of the problem in order to ensure greater clarity. This procedure, which is employed both for historical convention in the literature and to achieve numerical precision,

involves the use of specific values to non-dimensionalise quantities in the 2BP. The non-dimensionalizations quantities under consideration are

Physical constant	Unit	Value
Length unit	[km]	6378
Mass unit	[kg]	6×10^5
Time unit	[s]	806.785576

Table 3.1 Non-dimensionalizing values

Table 3.1 illustrates the values associated with the reference quantities. The characteristic length (l^*) is equal to the average radius of the Earth, the characteristic mass (m^*) is equal to the total weight of the fully loaded launch vehicle, and the characteristic time (t^*) is not directly imposed but calculated as

$$t^* = \sqrt{\frac{(l^*)^3}{\mu_\oplus}}. \tag{3.32}$$

With regard to the notation of the dimensionless quantities, the same notation as that introduced at the beginning of Chapter 2 is employed.

The EoMs, as presented in (2.23), can now be expressed in the ECEF RF, whereby the equations are projected along the three Cartesian coordinate axes. This results in a set of ODE, as follows

$$\frac{dx}{dt} = v_x \tag{3.33a}$$

$$\frac{dy}{dt} = v_y \tag{3.33b}$$

$$\frac{dz}{dt} = v_z \tag{3.33c}$$

$$\frac{dv_x}{dt} = -\frac{\mu_\oplus}{r^3} x + \frac{T_x}{m} + a_{D_x} + 2\omega_\oplus v_y + \omega_\oplus^2 x \tag{3.33d}$$

$$\frac{dv_y}{dt} = -\frac{\mu_\oplus}{r^3} y + \frac{T_y}{m} + a_{D_y} - 2\omega_\oplus v_x + \omega_\oplus^2 y \tag{3.33e}$$

$$\frac{dv_z}{dt} = -\frac{\mu_\oplus}{r^3} z + \frac{T_z}{m} + a_{D_z} \tag{3.33f}$$

$$\frac{dm}{dt} = -\frac{T}{c} \tag{3.33g}$$

The application of OCT to the set of ODEs (3.33) aims to identify the optimal control law that maximises the final mass. This in turn is equivalent to seeking the optimal payload during ascent of a launch vehicle. As previously stated in section 3.2, the preferred approach is Mayer's formulation, which reduces the problem statement by imposing $\Phi = 0$.

The state vector $\boldsymbol{x}(t) \in \mathbb{R}^n$ will consist of

$$\boldsymbol{x} = \left\{ \begin{matrix} x & y & z & u & v & w & m \end{matrix} \right\}^T. \tag{3.34}$$

In light of the fact that each state variable is associated with a corresponding adjoint variable, this leads to the creation of an augmented state vector $\boldsymbol{y}(t) \in \mathbb{R}^{2n}$

$$\boldsymbol{y} = \left\{ \begin{matrix} x & y & z & u & v & w & m & \lambda_x & \lambda_y & \lambda_z & \lambda_u & \lambda_v & \lambda_w & \lambda_m \end{matrix} \right\}^T. \tag{3.35}$$

The merit index is then defined as the final mass reached by the vehicle at the end of the ascent trajectory, namely

$$J = \varphi = m_f. \tag{3.36}$$

By explicitly defining each term present in the set of ODEs shown in equations (3.33), the formulation of the Hamiltonian is derived as follows

$$
\begin{aligned}
\mathcal{H} = \boldsymbol{\lambda}^T \boldsymbol{f} = \sum_{i=1}^{2n} \lambda_i f_i &= \lambda_r u + \lambda_\vartheta \frac{v}{r\cos\phi} + \lambda_\varphi \frac{w}{r} + \\
&\quad + \lambda_u \left[-\frac{\mu}{r^2} + \frac{v^2}{r} + \frac{w^2}{r} + \frac{T_u}{m} \right] + \\
&\quad + \lambda_w \left[-\frac{uv}{r} + \frac{vw}{r}\tan\varphi + \frac{T_v}{m} \right] + \\
&\quad + \lambda_w \left[-\frac{uw}{r} - \frac{v^2}{r}\tan\varphi + \frac{T_w}{m} \right] + \\
&\quad - \lambda_m \frac{T}{c},
\end{aligned}
\tag{3.37a}
$$

or rewritten in compact form

$$\mathcal{H} = \boldsymbol{\lambda}_r^T \boldsymbol{V} + \boldsymbol{\lambda}_V^T \left(\frac{\boldsymbol{T}}{m} - \mu \frac{\boldsymbol{r}}{r^3} \right) - \lambda_m \frac{T}{c}. \tag{3.38}$$

Grouping together all the terms that multiply the thrust-to-mass ratio, a new coefficient, referred to as the *Switching Function*, can be introduced:

$$\mathcal{S}_F = \boldsymbol{\lambda}_V^T \frac{\boldsymbol{T}}{T} - \lambda_m \frac{m}{c}. \tag{3.39}$$

The incorporation of the specified coefficient into Equation (3.38) enables the reformulation of this equation as follows

$$\mathcal{H} = \boldsymbol{\lambda}_r^T \boldsymbol{V} + \boldsymbol{\lambda}_V^T \left(-\mu \frac{\boldsymbol{r}}{r^3} \right) + \frac{T}{m} \mathcal{S}_F. \tag{3.40}$$

The control vector $\boldsymbol{u}(t)$ is a function of the thrust vector $\boldsymbol{T}$, both in terms of magnitude and direction. According to the PMP, the optimal control $\boldsymbol{u}^*$ that maximises the trajectory's merit index is the same that maximises the Hamiltonian, as demonstrated in Equation (3.40). It is evident from this equation that the Hamiltonian is a linear function of the thrust vector $\boldsymbol{T}$, and, as discussed in Section 3.2.2, this implies the adoption of a *bang-bang control* strategy. Therefore, the thrust should be maximised when $\mathcal{S}_F > 0$, resulting in $T = T_{max}$, whereas if $\mathcal{S}_F < 0$ the thrust shall be null $T = 0$. In this context, singular arcs, typically linked with atmospheric flight and and necessitate the calculation of the time derivatives of the switching function, are not considered.

With regard to the thrust vector $\boldsymbol{T}$, Lawden's work has made a significant contribution to the definition of the optimal thrust direction, which must be parallel to the adjoint velocity vector $\boldsymbol{\lambda}_V$, designated *primer vector*

$$\boldsymbol{\lambda}_V = \begin{Bmatrix} \lambda_u \\ \lambda_v \\ \lambda_w \end{Bmatrix}, \qquad \lambda_V = \|\boldsymbol{\lambda}_V\|. \tag{3.41}$$

The optimal thrust direction is that which maximises the $\mathcal{S}_F$ in Equation (3.39), thereby maximising the Hamiltonian, as described in Equation (3.40).

In light of the aforementioned considerations, equation (3.39) can be reformulated in scalar form

$$\mathcal{S}_F = \lambda_V^T - \lambda_m \frac{m}{c}. \tag{3.42}$$
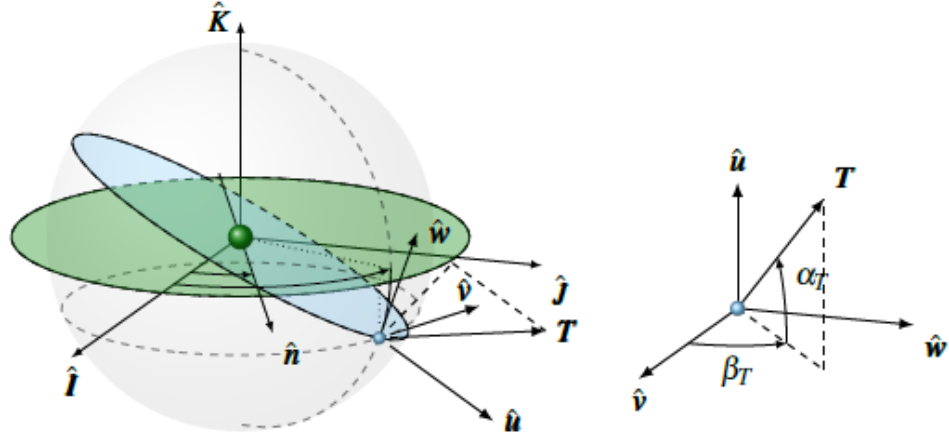
Fig. 3.2 SC ZEN RF and thrust angles [9]

Figure 3.2 presents the thrust vector $\boldsymbol{T}$ and its scalar decomposition angles, namely the elevation α_T and azimuth β_T angles, within the ZEN RF. Consequently, the thrust vector expressed in scalar form is

$$\boldsymbol{T} = \left\{ \begin{array}{c} T_u \\ T_v \\ T_w \end{array} \right\} = T \left\{ \begin{array}{c} \sin \alpha_T \\ \cos \alpha_T \cos \beta_T \\ \cos \alpha_T \sin \beta_T \end{array} \right\}, \qquad T = \|\boldsymbol{T}\|. \tag{3.43}$$

The optimal thrust angles are obtained by deriving the Hamiltonian equation (3.39) with respect to those same angles, resulting

$$\frac{\partial \mathcal{H}}{\partial \alpha_T} = 0 = \lambda_u \cos \alpha_T - (\lambda_v \cos \beta_T + \lambda_w \sin \beta_T) \sin \alpha_T \tag{3.44a}$$

$$\frac{\partial \mathcal{H}}{\partial \beta_T} = 0 = -\lambda_v \sin \beta_T + \lambda_w \cos \beta_T. \tag{3.44b}$$

Mathematical manipulations of Equation (3.43) lead to the derivation of optimal directions

$$\sin \alpha_T = \frac{\lambda_u}{\lambda_V} \tag{3.45a}$$

$$\cos \alpha_T \cos \beta_T = \frac{\lambda_v}{\lambda_V} \tag{3.45b}$$

$$\cos \alpha_T \sin \beta_T = \frac{\lambda_w}{\lambda_V}, \tag{3.45c}$$

52

which are the cosine directors of the primer vector and also correspond to the components of the thrust vector described in the equation (3.43). Consequently, the optimal thrust angles are derived by calculating the in-plane and out-of-plane angles using equations (3.45b) and (3.45c). Adjoint variables are obtained through the integration of the Euler-Lagrange equations, as indicated by equation (3.10).

Although the nature of the problem appears to be fully defined, the management of a highly non-linear dynamic system and the employment of a high-fidelity model introduce significant complexities in the automatic computation of thrust $S_F > 0$ and coast $S_F < 0$ phases. Therefore, small fluctuations in the S_F values close to zero can result in frequent sign changes during the integration process, which may give rise to numerical issues. Any alterations in the initial conditions during the correction process, even if minimal, could cause a sudden shift in the S_F and may either eliminate an essential boost phase or introduce an unwanted coast phase. Such changes might occur during the initial steps of integration, the resultant error gradient is likely to be computed with poor accuracy, thereby potentially preventing the solution from converging. One of the primary challenges in indirect optimization problems is the management of thrust discontinuities, as these can induce numerical issues in gradient evaluation. Various methods have been employed to address this issue, including smoothing techniques [28], homotopy and continuation approaches [29], uniform trigonometry methods [30], and integrated control regularization methods [31].

In the proposed analysis, an alternative approach is adopted in order to define the solution. The implementation of a TPBVP, within which an additional thrust arc is forcibly introduced, results in the formation of a Hybrid MPBVP (HMPBVP) in which the defined switching structure does not violate the PMP. The trajectories are idealised as divided into thrust sub-arcs whose duration is initially unknown and subject to optimisation. Furthermore, additional boundary conditions require that S_F be zero at the switching points where the thruster is activated or deactivated. Defining the switching structure in precise terms helps to obviate convergence issues and undesirable oscillations in the solution, thereby enhancing the effectiveness of the method in identifying an accurate result even when parts of S_F do not comply with the PMP.

this approach offers substantial numerical precision, an adequate rate of convergence for an indirect method - despite its dependence on the problem's complexity

- and greater robustness compared to other methods. Furthermore, the code is pre-compiled in $C{++}$ and employs the lsoda command for the integration phase, thereby markedly enhancing computational efficiency. This optimisation enables each iteration to be executed in less than a millisecond on a standard 2.60 GHz CPU, ensuring that solutions converge with an error tolerance of 1×10^{-8}.

Chapter 4

Ascent Trajectories in 2BP

Chapter 4 presents the results of ascent trajectories as a function of launch latitude. The existing launch sites have been considered as reference points, while each trajectory has been calculated using the 2BP, in accordance with the detailed EoMs outlined in previous Chapters. The approach to the problem has been as a TPBVP, with the incorporation of internal conditions in order to simulate the staging phase of the launcher, thereby transforming it into a Hybrid Multi-point Boundary Value Problem (HMPBVP). The relevant parameters for the launcher, pertaining to each thrust arc, are outlined below:

Launcher parameters	Unit	Value
Initial mass m_0	[kg]	6e05
Specific Impulse I_{sp}	[s]	320
Thrust 1st stage Sea Level	[kN]	7605
Thrust 1st stage in Vacuum	[kN]	8227
Thrust 2nd stage in Vacuum	[kN]	981

Table 4.1 Launcher parameters

The single-shooting method adopted in the dynamic model under study identifies a solution within the search space, hence suggesting that the launcher should thrust in preferential directions. Although the implemented IM is capable of computing optimal thrust angles to minimise propellant consumption, it is of the utmost importance to define appropriate initial assumptions. This requires a thorough understanding of

the underlying dynamics of the launcher's ascent and orbital insertion, in order to guarantee the generation of suitable initial guesses.

The analysis is conducted for both minimum-time problems, where the influence of the switching function is not considered, and minimum-consumption problems, with the objective of comparing the solutions.

Here, the general conditions for the proposed problems are derived from empirical considerations. The following sections present a series of results pertaining to different scenarios, with a specific focus on the ascent of a launcher with varying initial conditions, namely the latitude starting from the equator. For the problem in question, a number of positions corresponding to different existing launch bases have been identified. To ensure the comprehensive analysis of all potential scenarios, the symmetrical positions in the opposite hemisphere have also been included, despite the absence of actual operational launch bases in those locations.

4.1 Boundary Conditions

4.1.1 Initial Conditions

Each launch is conducted within a time window that allows for the desired orbit to be achieved via a direct ascent, with an MLTAN of 0 deg, corresponding to a SSO with the AN at 12:00. The table below presents the various times of launch in Coordinated Universal Time (UTC) terms

Launch Bases	LAT	Epoch UTC
Guyana Space Centre, French Guiana	5.236°N	2024/03/21 08:31:52
Satish Dhawan Space Centre, India	13.731°N	2024/03/21 17:20:33
Cape Canaveral Space Station, USA	28.562°N	2024/03/21 06:37:42
Vandenberg Space Force Base, USA	34.742°N	2024/03/21 03:57:58
Jiuquan Satellite Launch Center, China	40.958°N	2024/03/21 18:40:41
Baikonur Cosmodrome, Kazakhstan	45.921°N	2024/03/21 16:12:18

Table 4.2 Times of Passage on the Prime Meridian for Various Launch Bases on 21/03/2024

For each launch base, the latitude data underwent a conversion from spherical to Cartesian coordinates. Due to the sensitivity of the code, the trajectory is divided

into two distinct phases. In the first phase, which simulated a purely vertical ascent, the integration of EoM was conducted using a simple approach until the launcher reached an altitude of 15 km. This resulted in a dynamic control of the launcher model's attitude being imposed. The resulting conditions are then used as new initial conditions with a view to determining optimal ascent trajectories.

$$\boldsymbol{x}_0 = \left\{ x, \ y, \ z, \ v_x, \ v_y, \ v_z \right\}^T. \tag{4.1}$$

In addition to the initial position and velocity values provided, initial guesses must be assigned to the supplementary variables introduced for the multiple IM, specifically:

$$\boldsymbol{\lambda}_0 = \left\{ \lambda_x, \ \lambda_y, \ \lambda_z, \ \lambda_{v_x}, \ \lambda_{v_y}, \ \lambda_{v_z} \right\}^T. \tag{4.2}$$

A variety of considerations may be made on the basis of the value assumed by each added variable. For example, the position co-states, which quantify the impact on the evolution of the body's position quantities over time, demonstrate positive increasing values in the x and z directions, reflecting the trajectory of the launch vehicle ascent. Instead, considering the velocity co-states, the sign indicates whether the body is accelerating (for positive values) or decelerating (for negative values) along a specific direction, while the magnitude defines the relevance of the corresponding state quantity at that moment. Among the various added velocity variables, the one with the greatest magnitude identifies the most significant thrust direction. The last co-state, which is assumed to have a negative sign, defines the evolution of mass over time, providing insight into the propellant consumption. For the assignment of initial values, small non-zero values within the range of $10^{-2} \div 10^{-3}$ is used, with gradual adjustments made to guide the solution towards convergence.

The final piece of information concerns the variation in thrust that occurs at different phases of ascent. In the initial phase, the thrust is determined by the sea-level value that is required for lift-off from the Earth's surface. Subsequently, the thrust generated by the launcher's engines increases gradually in accordance with the decrease in atmospheric pressure. Ultimately, the second stage thrust, operating in a vacuum, is initiated following a specific mission duration, once the first stage propellant is depleted. Despite the aforementioned model exhibiting three thrust phases, resulting in a MBPVB, it has been modelled as a TBPVB by enforcing thrust variation conditions to simulate the launcher's adaptation and staging.

4.1.2 Final Conditions

Ascent trajectories are considered complete upon the fulfilment of the designated final conditions, which correspond to the insertion into the target orbit. The final conditions are defined in terms of Keplerian parameters that describe the orbit. Accordingly, the provided data include

Orbital Parameters	Unit	Value
Semi-major axis (a)	[km]	6858
Eccentricity (e)		0
Inclination (i)	[deg]	97.2
RAAN (Ω)	[deg]	0

Table 4.3 Target orbit parameters

The rationale behind the imposition of final conditions in relation to orbital parameters is closely linked to the implementation of transversality conditions within the model. The study [32] demonstrated that reduced transversality conditions, aimed at eliminating unknown multipliers, are derived with regard to the free orbital parameters. This approach has consequently enhanced the robustness of the code and the speed of convergence. Consequently, in this analysis, the true anomaly (ν_f) is selected as the free parameter, thus enabling the insertion point into orbit to be determined by the optimal solutions, as opposed to being predefined. It should be noted that the final conditions of the implemented process are converted to Cartesian coordinates. This conversion in coordinates involves a transition from the perifocal RF to the ECEF RF, utilising the rotation matrices described in Chapter 2. Although the assignment in Keplerian elements is the preferred option due to the reduced transversality conditions, the conversion back to Cartesian coordinates is the favoured approach as it allows for the EoM of the problem to be easily stated.

The set of final boundary conditions can be stated as:

$$\boldsymbol{\chi}_f = \{a,\ e,\ i,\ \Omega,\ \lambda_m\}^T \tag{4.3}$$

where these conditions remain unchanged across the various mission configurations examined. Given that the objective was to minimise propellant usage, the parameter to be optimised is the final mass m_f. This condition is imposed by assigning a value of 1 to the associated co-state λ_{m_f}, as derived from the optimality conditions

discussed in Chapter 3. Furthermore, the operating time is not constrained, thereby allowing the t_f to be computed freely.

4.2 Results

The optimal ascension trajectory can now be presented with the accompanying results. It would be particularly beneficial at this point to examine the magnitude of velocity experienced throughout the entirety of the ascension phase.
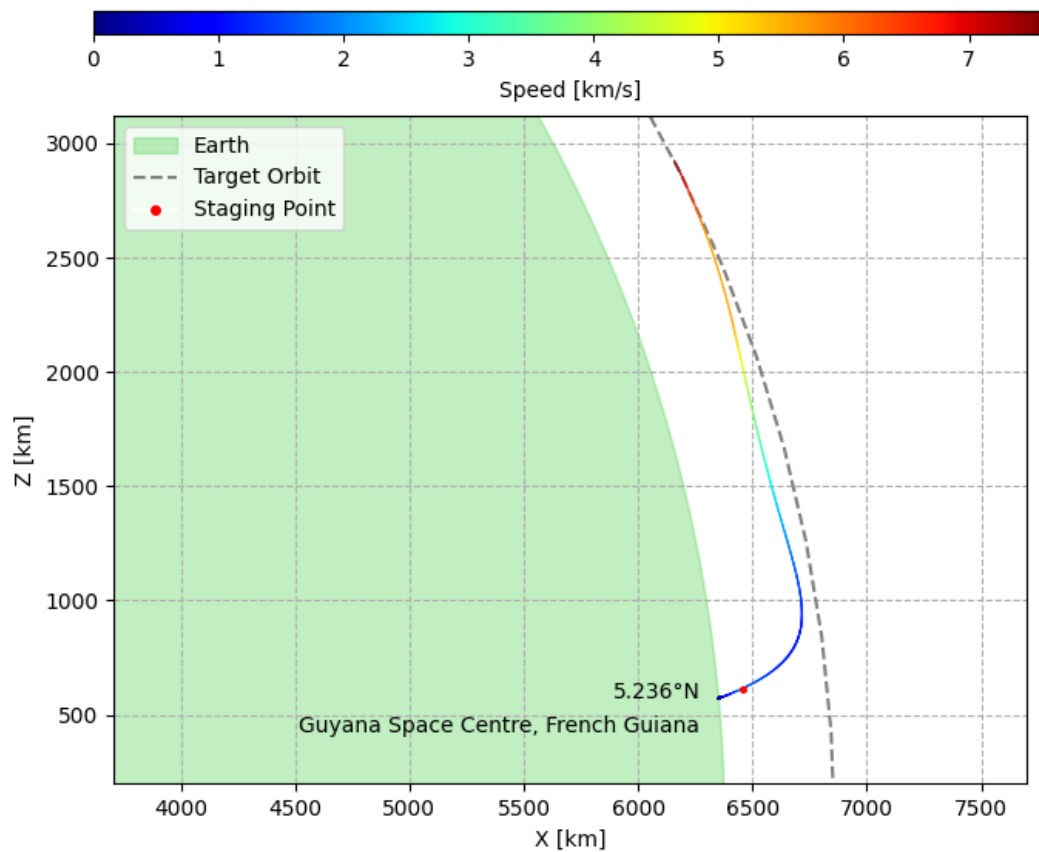
Fig. 4.1 Magnitude of velocity experienced throughout the ascent trajectory

Figure 4.1 illustrates the evolution of the launcher's relative velocity along its trajectory. Initially, at the point where the launcher is situated on Earth's surface, its velocity is equal to zero. As the launcher ascends, its velocity demonstrates a progressive increase, initially in radial direction until it reaches the magnitude of the

orbital velocity

$$V_{orbit} = \sqrt{\frac{\mu_E}{a}} = 7.62377 \; \frac{km}{s} \;. \tag{4.4}$$

Following an analysis of the evolution of the launcher's velocity, optimal ascent trajectories for the various launch sites under consideration are presented. The trajectories have been calculated on the basis of the specific initial conditions of each site and the constraints imposed by the mission configurations.
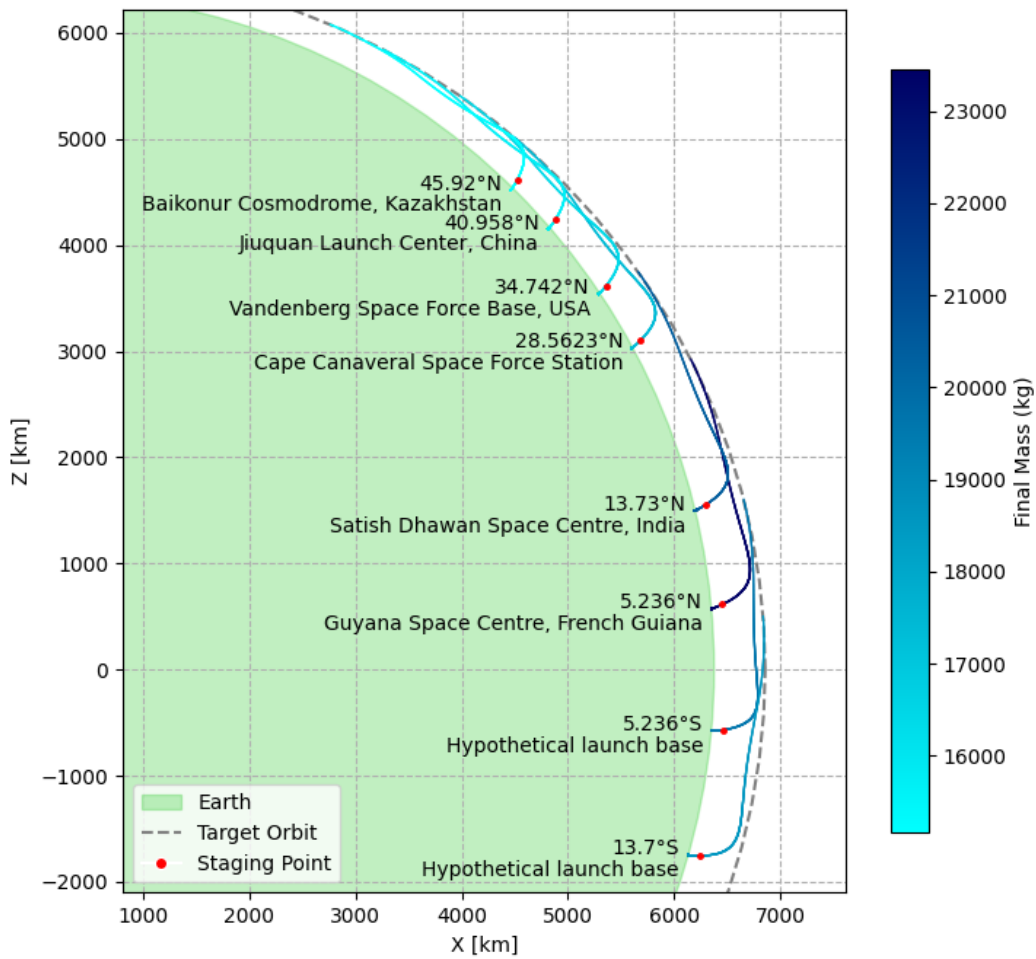
Fig. 4.2 Optimal ascent trajectories of each launch sites

Figure 4.2 reveals that the optimal trajectory, in terms of final mass, is achieved by launching from the Guyana Space Centre, situated at 5.236 deg N. A comparison of the results reveals that, for this specific type of implementation problem, the cost in propellant consumption increases as the launch point moves further away from

the Equator. Consequently, launches closer to the Equator offer greater benefits due to the maximum intensity of the Earth's rotational effect, which diminishes with increasing latitude. This results in a high initial absolute velocity for the launcher, which is advantageous for computing the optimal solution. It would be beneficial to give greater attention to the optimal trajectories obtained in the most and least advantageous cases.
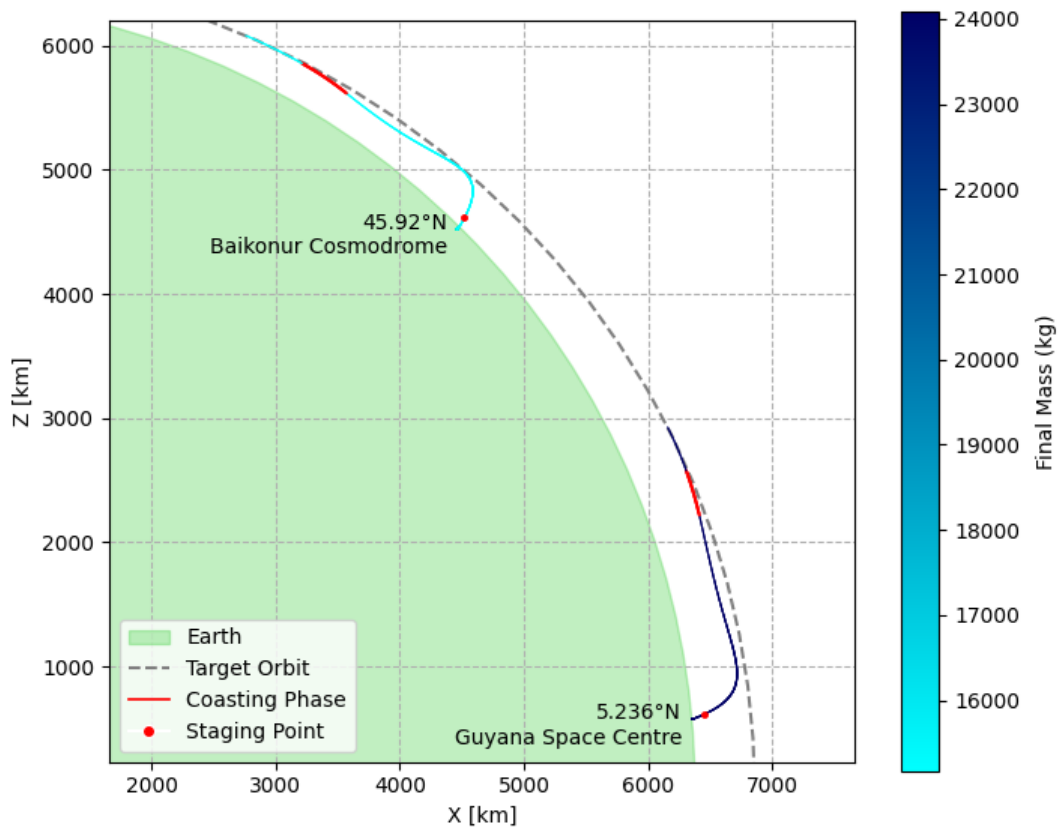
Fig. 4.3 Comparison between the 5.23 deg N and 45.92 deg N solutions

As illustrated in Figure 4.3, while the trajectories display comparable patterns, they also exhibit notable distinctions. In the most advantageous case, the trajectory does not reach the orbit immediately after the gravity turn phase, but rather gradually increases its velocity until the phase of insertion into the orbit. Conversely, the 45.92 degree N trajectory initially reaches the orbit but subsequently loses altitude due to the force of gravity, which is then regained through an additional increase in velocity. Another significant distinction pertains to the coasting phase, which occurs at different points during the ascent and has varying durations.

It is now possible to analyse the propellant expenditure.
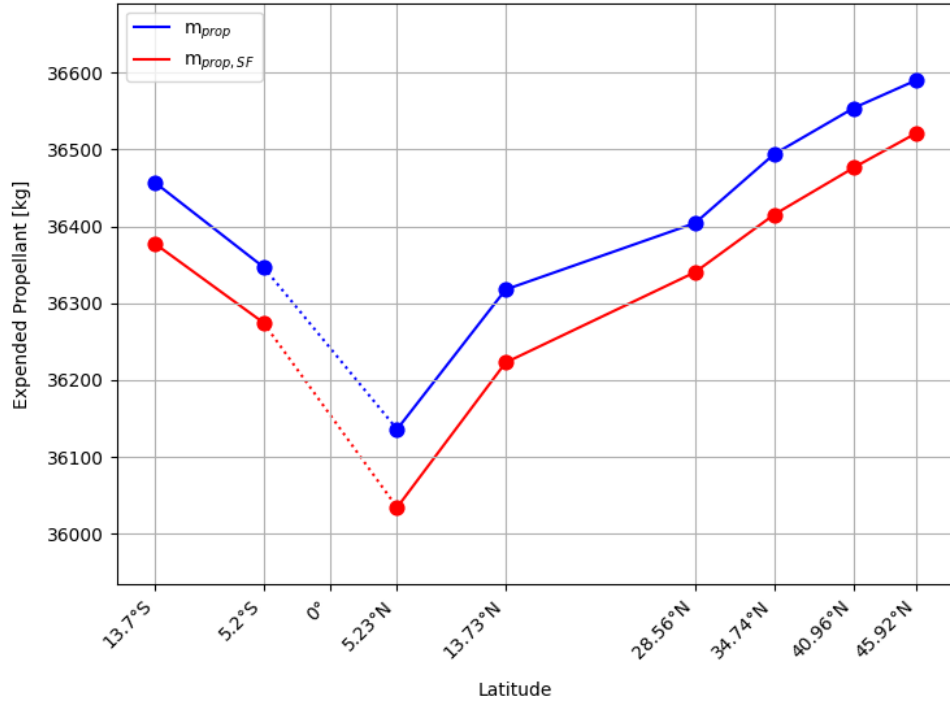
Fig. 4.4 Propellant consumption as LAT varies

Figure 4.4 clearly demonstrates that the enabling of the $\mathcal{S}_F$ results in a considerable reduction in propellant expenditure. Consequently, an increase in the duration of the mission, which effectively transforms the problem from a minimum time to a minimum consumption, gives rise to solutions that achieve approximately a 7% reduction in stored propellant mass. Given the sensitivity of the code, it was not feasible to analyse the ascent towards the South; instead, the analysis was limited to that towards the North. This explains why the expected results are not symmetrical, demonstrating that changing the launch hemisphere is not advantageous, and that, in some scenarios, launches towards the South are considered.

Now that the propellant consumption required to complete the mission across different architectures has been quantified, it is essential to examine the influence of the velocity co-states assigned within each scenario to ascertain their impact on mission performance. A comprehensive analysis of these co-states will facilitate a deeper understanding of how velocity adjustments contribute to overall mission

efficiency, thereby enabling a more informed evaluation of the mission's dynamic behaviour.
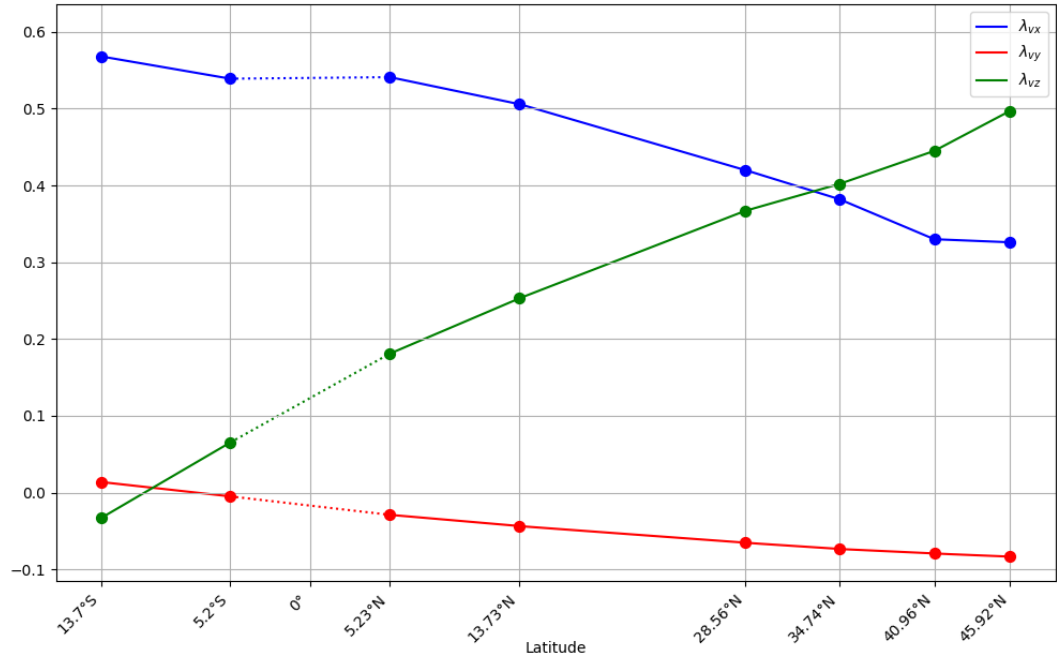
Fig. 4.5 Initial guesses of co-states of velicity as LAT varies

As illustrated in Figure 4.5, the magnitude of λ_{v_y} is found to be negligible in comparison to the other two components. As previously stated, the preferential thrust directions are along the radial direction and northward, given that the predominant contributions are λ_{v_x} and λ_{v_z}. The graph clearly demonstrates that as one moves away from the equator, the parameters in question decrease and increase, respectively. Upon combining the various components, it becomes evident that the cost of conducting a direct launch is significantly higher at higher latitudes, thereby confirming the initial observations.

In considering the optimal solutions, it is observed that the solution with the lowest propellant consumption shows a significant predominance of the radial direction throughout the evolution of the launcher. To provide a clearer understanding of the thrust direction's evolution during the ascent phase, the temporal trends of the thrust angles, α_T and β_T, for this specific case are analysed and presented. This detailed analysis offers insights into the dynamic behavior of the thrust vector, highlighting its influence on the efficiency and performance of the ascent trajectory.
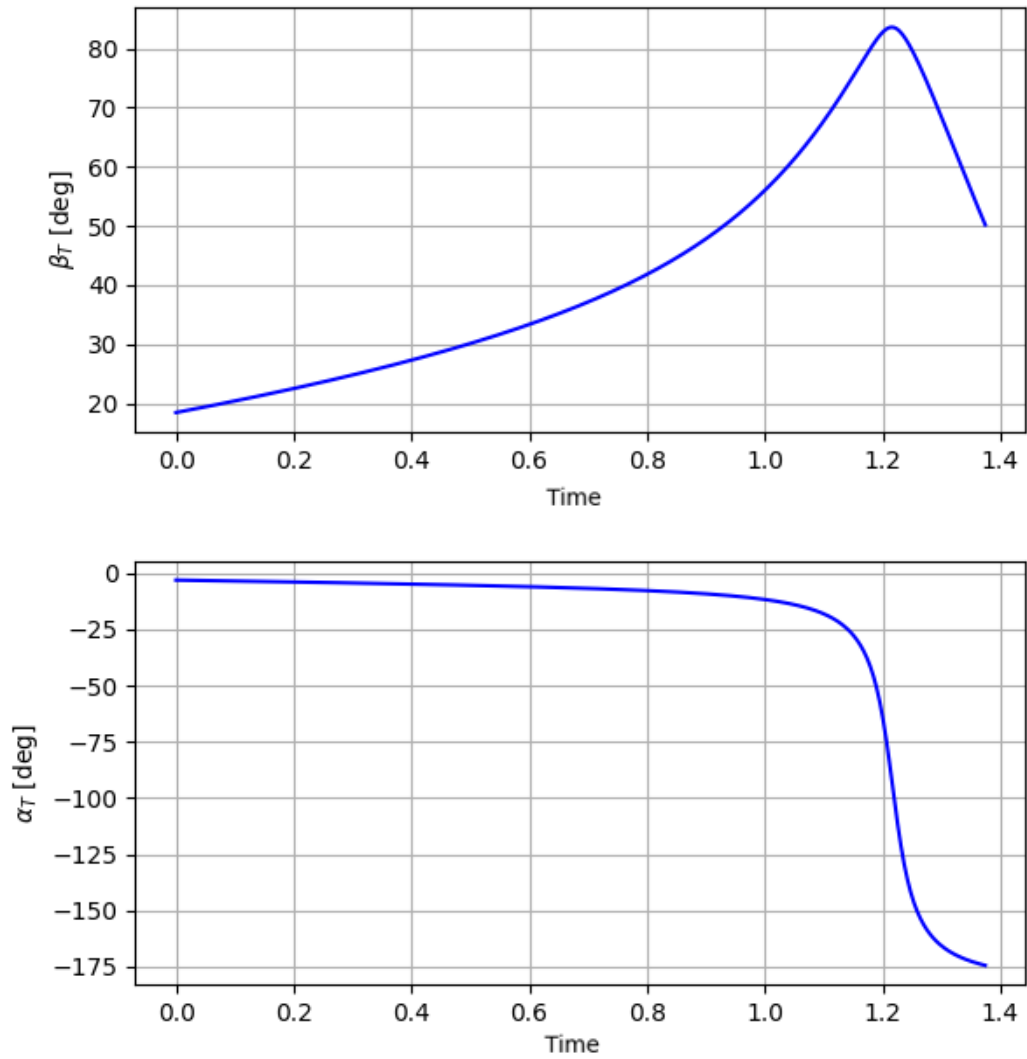
Fig. 4.6 Evolution of the thrust angles, α_T and β_T, with respect to non-dimensional time t^*

By considering the launch trajectory originating from French Guiana, it is feasible to conduct a detailed analysis of the evolution of the orbital parameters over time. This analysis facilitates a comprehensive comprehension of the launcher behaviour during its ascent and orbital insertion, offering precise insights into the variations of each orbital parameter throughout the flight trajectory.

Semimajor axis

Eccentricity

Inclination
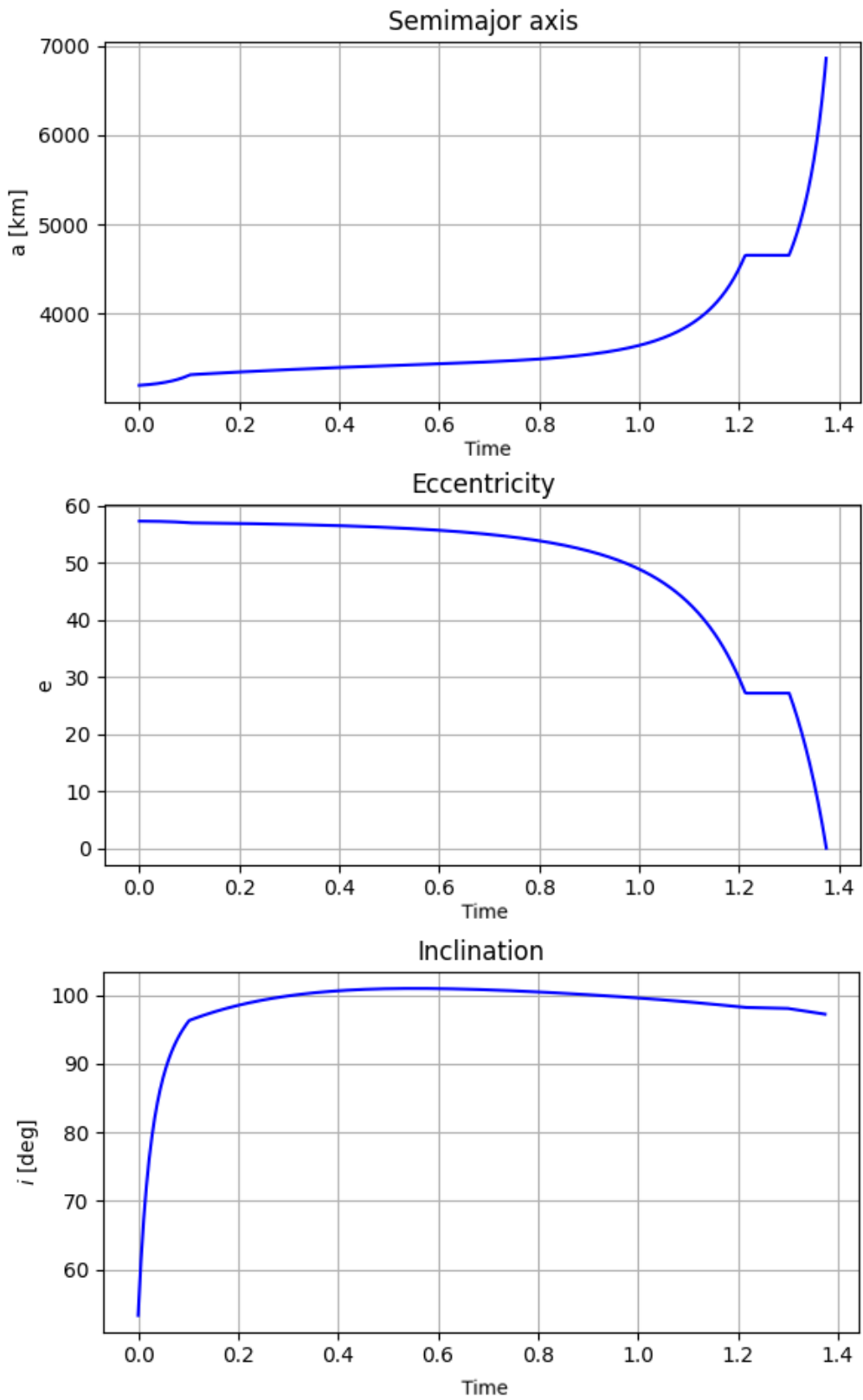
Fig. 4.7 Evolution of the orbit parameters with respect to non-dimensional time t^*

As illustrated in Figure 4.7, the launcher successfully reaches the desired final orbit from a specific initial condition. Furthermore, a constant segment is evident, indicating a non-propulsive phase during which the orbital parameters remain unchanged. This phase occurs when $\mathcal{S}_F < 0$, as further illustrated in Figure 4.8.
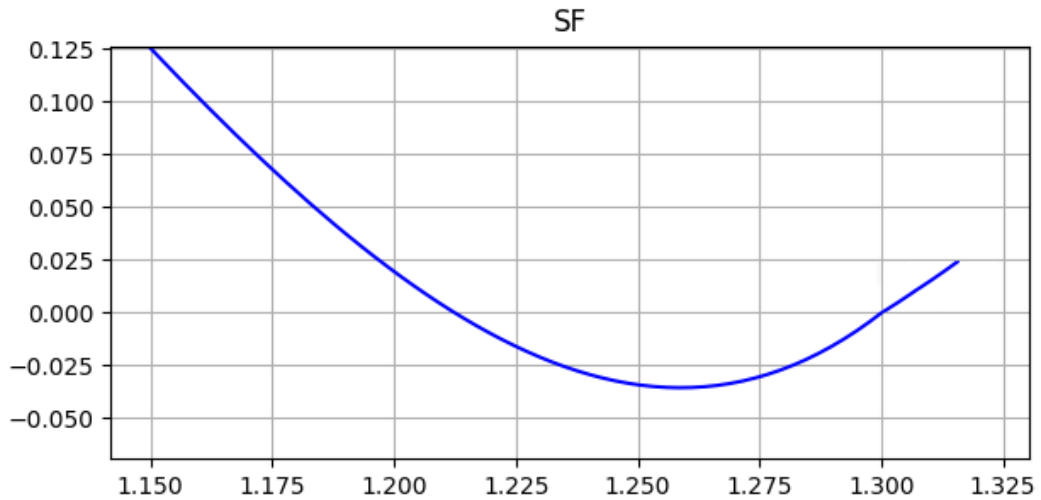
Fig. 4.8 Switching function behaviour over non-dimensional time t^*

Accordingly, the non-propelled phase may be more effectively visualised through the utilisation of total mass along the trajectory. This trend clearly highlights the coasting phase, during which there is no consumption of propellant as the thrust is switched to zero.
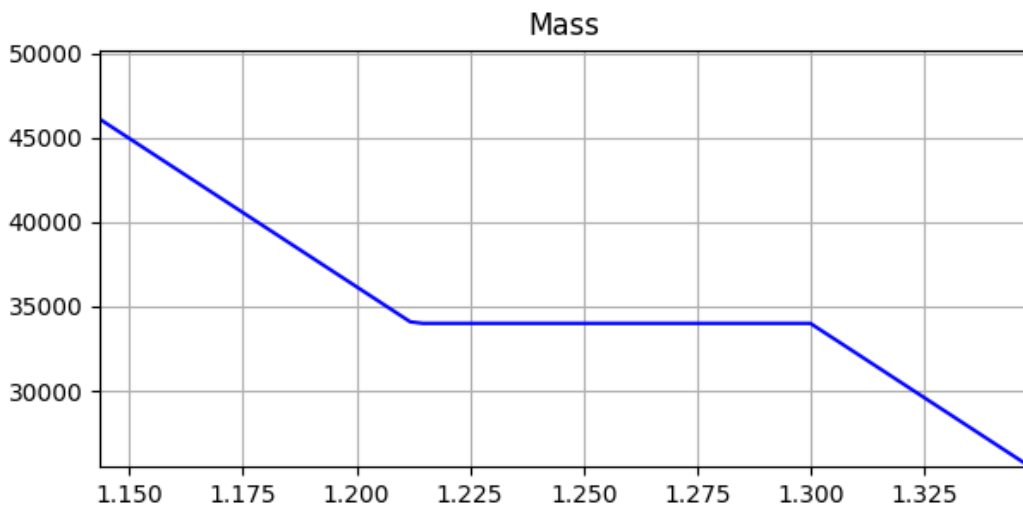
Fig. 4.9 Trend of mass in the range where $\mathcal{S}_F < 0$

Moreover, in consideration of the linear relationship between propellant consumption and thrust, as indicated by Equation (2.23c), a notable detail regarding the behaviour of the total mass becomes evident
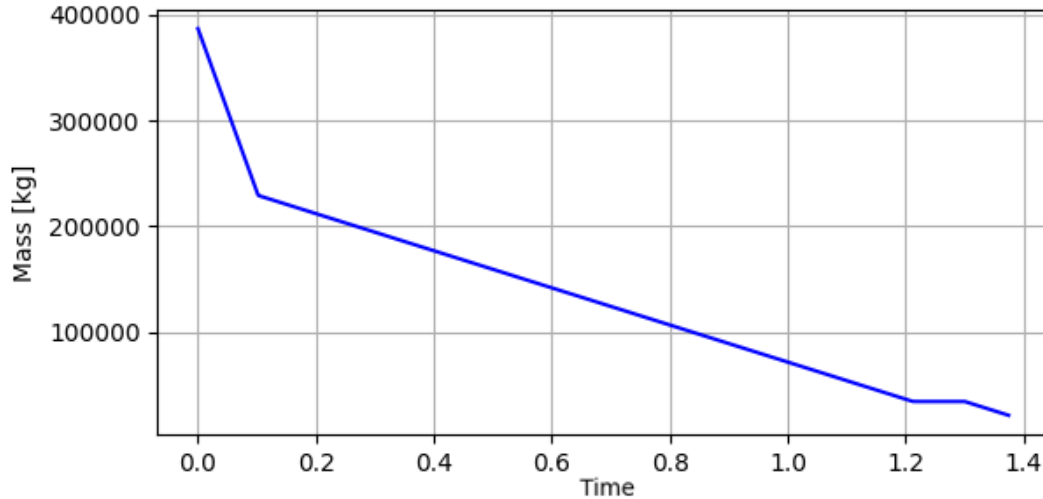
Fig. 4.10 Trend of mass behaviour over non-dimensional time t^*

Figure 4.10 reveals a change in the slope of the trend, indicative of a variation in the imposed thrust conditions. This implies that staging took place at that phase of the mission, signifying the transition from the first to the second stage.

Finally, it is of paramount importance to analyse the evolution of the heat flux during the ascent to identify the critical moments of the mission and the corresponding temperatures. This study allows for the evaluation of the launcher's safety and reliability, thus ensuring that structural components and ablative materials can withstand extreme thermal conditions. The behaviour of heat flux is determined by means of the following relationship, which takes into account density variation and relative velocity, namely:

$$Q = \frac{1}{2} \rho \, v_{rel}^3.$$ (4.5)

Equation (4.5) permits the definition of the thermal flux evolution throughout the entire ascent phase of the launcher, which develops as follows
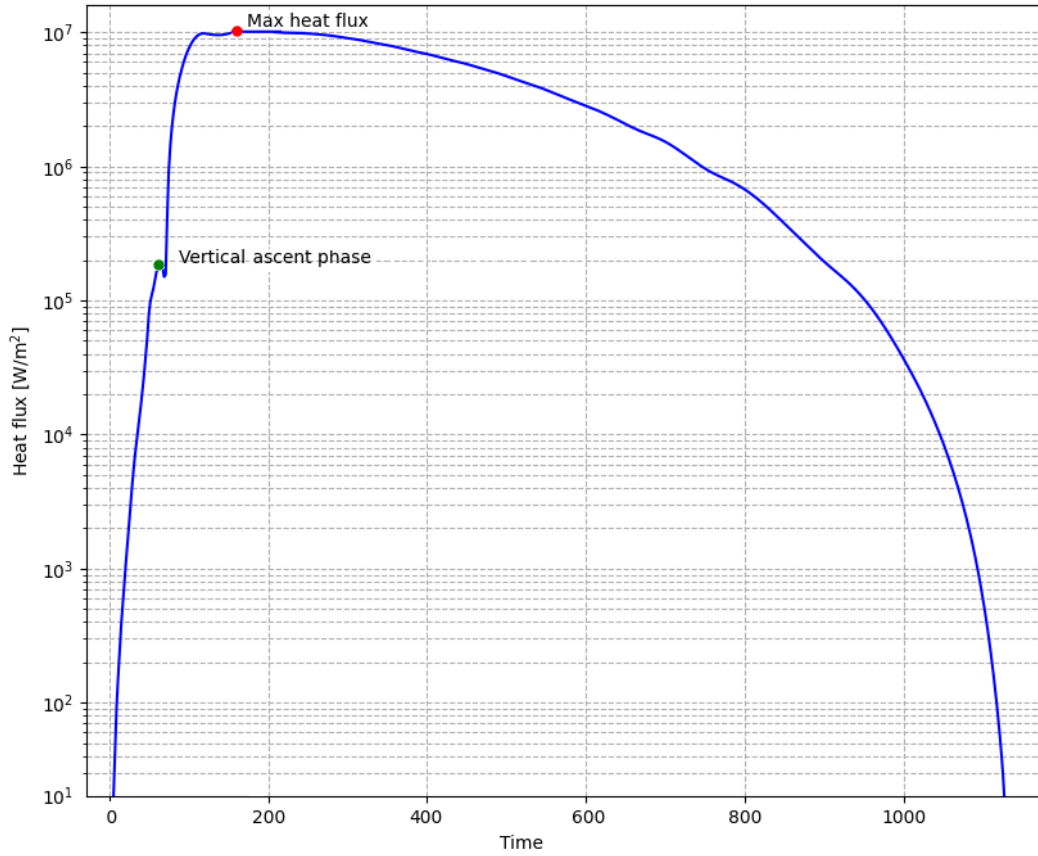
Fig. 4.11 Thermal flux evolution during mission operating times

As illustrated in Figure 4.11, the heat flux demonstrates a clear upward trend during the ascent phase. Initially, this increase occurs at a relatively rapid rate, driven by the combined effects of velocity and aerodynamic compression. Once the maximum value is reached, a decline in the heat flux is evident as the launcher traverses the denser layers of the atmosphere, leading to a reduction in aerodynamic friction. Two points of interest can be identified: firstly, at the end of the vertical ascent phase, where the heat flux reaches its initial peak value, and secondly, at the peak heat flux value itself. By reference to the Stefan–Boltzmann law (4.6), it is possible to ascertain the temperatures experienced by the launcher during these specific phases, thus providing a detailed understanding of the thermal conditions encountered during the flight.

$$Q = \sigma \, \varepsilon \left(T^4 - T_{env}^4 \right) \tag{4.6}$$

The Stefan-Boltzmann constant (σ), in conjunction with the emissivity values of the materials (ε) and the thermal flux values, allows for the determination of temperatures at specific points of interest, which are found to be 1469.873 K and 3284.687 K.

Given the sensitivity of the case, the analysis focuses on the ascent phase, without going into detail on thermal analysis, which is beyond the scope of this thesis. In order to avoid any structural compromise as a result of the high temperatures that are likely to be experienced during ascent, two potential strategies could be contemplated. The first approach involves the utilisation of ablative coating materials, whereby these materials evaporate at specific temperatures, thereby reducing the surface temperature and protecting the underlying structure. The second approach is the implementation of thrust throttling, which, although it increases mission duration, allows for a significant reduction in surface temperature, thus ensuring the structural integrity of the vehicle. Furthermore, the division of the ascent trajectory into two segments has no impact on the thermal flux outcomes, demonstrating the consistency and reliability of the solution. Consequently, the results obtained are considered representative of real-world conditions, providing a robust basis for further analysis and optimisation of the ascent phase.

Chapter 5

Conclusion

In light of the growing interest in Sun-Synchronous Orbits (SSO), there is a need for more comprehensive investigations into their dynamics, as well as the development of effective methodologies to optimise trajectories for entering such orbits. In this context, this thesis presents an in-depth study with the objective of optimising ascent trajectories for launching satellites into SSOs.

Indirect methods have been identified as the most appropriate approach to resolving the complex and multifaceted Hamiltonian Boundary Value Problem (HBVP) inherent to the application of Optimal Control Theory (OCT) to ascent trajectory optimisation. Pontryagin's Maximum Principle was instrumental in defining the optimal control strategies necessary for minimising propellant consumption. This thesis, therefore, has been structured to identify the optimal solution, with a view to minimising propellant consumption while maximising payload capacity. In order to achieve this, various factors must be taken into consideration, including launch bases, mission architectures and dynamic models. The study commenced with the creation of a bespoke simulation scenario, designed to model the ascent of a launch vehicle into a low Earth OCT. A robust dynamic model was developed, incorporating the primary gravitational influence of the Earth along with perturbative effects such as atmospheric drag, utilising the Harris-Priester atmospheric density model. The requisite and optimal conditions were thus derived, offering valuable insights that guide the evolution of the control law toward its optimal configuration. The derivation of optimality conditions for defining the Two-Point Boundary Value Problem (TPBVP) and the subsequent analysis of solutions afforded a comprehensive understanding

of the potential ascent configurations of the model. The sensitivity of the indirect method was addressed through the implementation of tailored strategies, including the introduction of two distinct thrust arcs to simulate staging, the a priori definition of a thrust structure, and the separation of the initial purely vertical ascent phase to impose dynamic control within the model, thereby mitigating numerical issues.

The indirect approach, which is distinguished by its considerable computational speed, allows for an expeditious assessment of a multitude of ascent scenarios under diverse initial conditions. The results demonstrate that the selection of the launch base has a considerable impact on mission performance, with a direct effect on propellant consumption. The analyses demonstrated that launch bases situated in proximity to the equator tend to exhibit enhanced efficiency, predominantly due to the augmented initial velocity imparted by Earth's rotational motion. Notwithstanding the simplifications introduced in the model as a result of the implementation of a two-body problem with a restricted number of perturbations, the theoretical model demonstrated a satisfactory degree of accuracy. This has resulted in the development of an effective baseline model for the planning, verification, and optimisation of future missions. The accuracy of the model was validated by comparing its predictions with actual data from a SpaceX launch, with particular focus on propellant expenditure and mission timing.

5.1 Future work

The objectives of this thesis have been fulfilled by the identification of appropriate solutions to the case study. An indirect optimisation approach was employed for the ascent trajectories, thereby providing effective solutions for the management of model sensitivity issues. This study has facilitated an understanding of the potential ascent strategies, which are contingent upon the mission objectives.

Given the extensive scope of the subject matter, it was not feasible to examine all elements in exhaustive detail. It would thus be beneficial to investigate certain elements further in order to enhance the fidelity of the model, thereby progressing from a medium-fidelity model to a high-fidelity one. Firstly, an essential improvement is the implementation of a more accurate atmospheric density model, in order to more precisely capture the effects it introduces on the model during both ascent and varying launch days, with a comprehensive consideration of solar activity. Furthermore,

the incorporation of additional perturbative effects, such as the Earth's non-spherical shape (the second most significant perturbation), as well as gravitational interactions with other celestial bodies and the impact of solar radiation pressure, is of paramount importance.

Further enhancements to the model and its implementation can be achieved by transitioning from a TPBVP to a MPBVP for simulating staging. This involves imposing the values associated with each stage in each thrust arc to identify the optimal pattern. The configuration of the launch vehicle in multiple stages is of great consequence for the optimal utilisation of propellant. The progressive reduction of mass through stage separation enables a more efficient ascent. This highlights the significance of meticulous staging strategies in trajectory optimisation. Furthermore, a crucial element is the thermal study, which offers a more comprehensive insight into operational conditions and thermal stresses on materials. Ultimately, adopting an ascent model that progressively aligns with real-world dynamics by incorporating not only direct manoeuvres but also non-propelled stationary phases, plane changes, and insertions, enabling dynamic trajectory adjustments, can further enhance the model.

These refinements will not only bring the model closer to reality but also enhance its stability and robustness, thereby providing a solid foundation for the planning, verification, and optimisation of future missions. These improvements will significantly contribute to the increased accuracy and reliability of simulations, thus ensuring that the model can be confidently used in a wide range of operational scenarios.

References

[1] KE Tsiolkovsky. Exploration of the world spaces by reactive devices:(reprinting works of 1903 and 1911 with some changes and additions). *Kaluga: 1st Guest. GSNH*, 1926.

[2] Richard S Johnston and Wayland E Hull. Apollo missions. *Biomedical Results of Apollo, eds RS Johnston, LF Dietlein and C. Berry (Washington, DC: National Aeronautics and Space Administration)*, pages 9–40, 1975.

[3] Nick Scoville, RG Abraham, H Aussel, JE Barnes, A Benson, AW Blain, D Calzetti, A Comastri, P Capak, C Carilli, et al. Cosmos: Hubble space telescope observations. *The Astrophysical Journal Supplement Series*, 172(1):38, 2007.

[4] Davide Sivolella. *The space shuttle program: Technologies and accomplishments*. Springer, 2017.

[5] SpaceX. Falcon 9, 2024.

[6] Blue Origin. New glenn: The foundation for a new era, 2024.

[7] Luigi Grippo, Marco Sciandrone, Luigi Grippo, and Marco Sciandrone. Metodo di newton. *Metodi di ottimizzazione non vincolata*, pages 165–205, 2011.

[8] eoPortal: Earth Observation Missions. Iceye microsatellites constellation, 2024.

[9] Mascolo Luigi. *Low-Thrust Optimal Escape Trajectories from Lagrangian Points and Quasi-Periodic Orbits in a High-Fidelity Model*. PhD thesis, 2023.

[10] Hartmut Wziontek, Sylvain Bonvalot, Reinhard Falk, Germinal Gabalda, Jaakko Mäkinen, Vojtech Pálinkás, Axel Rülke, and Leonid Vitushkin. Status of the international gravity reference system and frame. *Journal of Geodesy*, 95(1):7, 2021.

[11] Jet Propulsion Laboratory Solar System Dynamics. Jpl planetary and lunar ephemerides: Export information, 2024.

[12] John E Prussing and Bruce A Conway. *Orbital mechanics*. Oxford University Press, USA, 1993.

References

[13] Emre ÜNAL. Launch vehicle design, modeling and trajectory optimization. 2021.

[14] EZGİ CİVEK COŞKUN. Multistage launch vehicle design with thrust profile and trajectory optimization. 2014.

[15] Sangtae Kim Sung Wook Paek. Sun-synchronous repeat ground tracks and other useful orbits for future space missions. 2019.

[16] Ronald J Boain. Ab-cs of sun-synchronous orbit mission design. 2004.

[17] Noble Hatten and Ryan P Russell. A smooth and robust harris-priester atmospheric density model for low earth orbit applications. *Advances in Space Research*, 59(2):571–586, 2017.

[18] Leonhard Euler. Elementa calculi variationum. *Novi commentarii academiae scientiarum Petropolitanae*, pages 51–93, 1766.

[19] Mikhail Ivanov Krastanov, NK Ribarska, and Ts Y Tsachev. A pontryagin maximum principle for infinite-dimensional problems. *SIAM Journal on Control and Optimization*, 49(5):2155–2182, 2011.

[20] Richard Ernest Bellman and Robert S Roth. *The Bellman continuum: a collection of the works of Richard E. Bellman*. World Scientific, 1986.

[21] John T Betts. *Practical methods for optimal control and estimation using nonlinear programming*. SIAM, 2010.

[22] Guido Colasurdo and Dario Pastrone. Indirect optimization method for impulsive transfers. In *Astrodynamics Conference*, page 3762, 1994.

[23] Lorenzo Casalino, Guido Colasurdo, S Data, D Pastrone, et al. Traiettorie ottimali di ascesa in orbita. In *XII Congesso Nazionale AIDAA, Como, Villa Olmo, Italy*, volume 2, pages 1419–1429. 1993.

[24] Frank H Clarke. The generalized problem of bolza. *SIAM Journal on Control and Optimization*, 14(4):682–699, 1976.

[25] James Phillip McDanell and William Francis Powers. Necessary conditions joining optimal singular and nonsingular subarcs. *SIAM Journal on Control*, 9(2):161–173, 1971.

[26] SciPy Community. scipy.integrate.LSODA, 2024.

[27] AP Hayes. The adams-bashforth-moulton integration methods generalized to an adaptive grid. *arXiv preprint arXiv:1104.3187*, 2011.

[28] Cristiana Silva and Emmanuel Trélat. Smooth regularization of bang-bang optimal control problems. *IEEE Transactions on Automatic Control*, 55(11):2488–2499, 2010.

References

[29] Zhijie Gao and Hexi Baoyin. Using homotopy method to solve bang–bang optimal control problems. *Optimization, Simulation, and Control*, pages 243–256, 2013.

[30] Kshitij Mall, Michael J Grant, and Ehsan Taheri. Uniform trigonometrization method for optimal control problems with control and state constraints. *Journal of Spacecraft and Rockets*, 57(5):995–1007, 2020.

[31] Casey R Heidrich, Michael J Sparapany, and Michael J Grant. Investigation of control regularization functions in bang-bang/singular optimal control problems. In *AIAA Scitech 2021 Forum*, page 2037, 2021.

[32] Binfeng Pan, Zheng Chen, Ping Lu, and Bo Gao. Reduced transversality conditions in optimal space trajectories. *Journal of Guidance, Control, and Dynamics*, 36(5):1289–1300, 2013.

Appendix A

Euler-Lagrange equations for the adjoint variables

$$\frac{d\lambda_x}{dt} = \left(\frac{\mu_\oplus}{r^{3/2}} - \frac{3\,\mu_\oplus\,x^2}{r^{5/2}} \right) \lambda_{v_x} - \frac{3\,\mu_\oplus\,x}{r^{5/2}} (\lambda_{v_y} y + \lambda_{v_z} z)$$

$$\frac{d\lambda_y}{dt} = \left(\frac{\mu_\oplus}{r^{3/2}} - \frac{3\,\mu_\oplus\,y^2}{r^{5/2}} \right) \lambda_{v_y} - \frac{3\,\mu_\oplus y}{r^{5/2}} (\lambda_{v_x} x + \lambda_{v_z} z)$$

$$\frac{d\lambda_z}{dt} = \left(\frac{\mu_\oplus}{r^{3/2}} - \frac{3\,\mu_\oplus\,z^2}{r^{5/2}} \right) \lambda_{v_z} - \frac{3\,\mu_\oplus\,z}{r^{5/2}} (\lambda_{v_x} x + \lambda_{v_y} y)$$

$$\frac{d\lambda_{v_x}}{dt} = -\lambda_x \qquad\qquad\qquad\qquad\qquad\qquad\text{(A.1)}$$

$$\frac{d\lambda_{v_y}}{dt} = -\lambda_y$$

$$\frac{d\lambda_{v_z}}{dt} = -\lambda_z$$

$$\frac{d\lambda_m}{dt} = \frac{T}{m^2} \sqrt{\lambda_{v_x}^2 + \lambda_{v_y}^2 + \lambda_{v_z}^2}$$